AGU ADVANCING EARTH AND SPACE SCIENCE

JGR Solid Earth

RESEARCH ARTICLE

10.1029/2022JB024497

Using Misorientation and Weighted Burgers Vector Statistics to Understand Intragranular Boundary Development and Grain Boundary Formation at High Temperatures

Sheng Fan[1,2], John Wheeler[3], David J. Prior[1], Marianne Negrini[1], Andrew J. Cross[4], Travis F. Hager[5], David L. Goldsby[5], and David Wallis[2]

[1]Department of Geology, University of Otago, Dunedin, New Zealand, [2]Department of Earth Sciences, University of Cambridge, Cambridge, UK, [3]Department of Earth and Ocean Sciences, University of Liverpool, Liverpool, UK, [4]Department of Geology and Geophysics, Woods Hole Oceanographic Institution, Woods Hole, MA, USA, [5]Department of Earth and Environmental Science, University of Pennsylvania, Philadelphia, PA, USA

Key Points:

- We propose that intragranular boundaries form via the intersection of boundary segments containing dislocations with distinct slip systems
- Subgrain rotation can operate to large misorientation angles (~38°) with rational, low-order misorientation axes (*a* and *m* axes)
- Boundary misorientation axes become randomized from additional mechanisms (e.g., grain boundary sliding) following grain boundary formation

Supporting Information:

Supporting Information may be found in the online version of this article.

Correspondence to:

S. Fan,
sheng.fan@otago.ac.nz;
sf726@cam.ac.uk

Citation:

Fan, S., Wheeler, J., Prior, D. J., Negrini, M., Cross, A. J., Hager, T. F., et al. (2022). Using misorientation and weighted Burgers vector statistics to understand intragranular boundary development and grain boundary formation at high temperatures. *Journal of Geophysical Research: Solid Earth*, *127*, e2022JB024497. https://doi.org/10.1029/2022JB024497

Received 30 MAR 2022
Accepted 29 JUL 2022

Author Contributions:

Conceptualization: Sheng Fan, David J. Prior
Data curation: Sheng Fan, Marianne Negrini, Andrew J. Cross, Travis F. Hager
Formal analysis: Sheng Fan
Funding acquisition: Sheng Fan, David J. Prior
Methodology: Sheng Fan, John Wheeler, David J. Prior, Andrew J. Cross
Software: Sheng Fan, John Wheeler
Supervision: John Wheeler, David J. Prior, David L. Goldsby
Writing – original draft: Sheng Fan

Abstract

During plastic deformation, strain weakening can be achieved, in part, via strain energy reduction associated with intragranular boundary development and grain boundary formation. Grain boundaries (in 2D) are segments between triple junctions, that connect to encircle grains; every boundary segment in the encircling loop has a high (>10°) misorientation angle. Intragranular boundaries terminate within grains or dissect grains, usually containing boundary segments with a low (<10°) misorientation angle. We analyze electron backscatter diffraction (EBSD) data from ice deformed at −30°C ($T_h \approx 0.9$). Misorientation and weighted Burgers vector (WBV) statistics are calculated along planar intragranular boundaries. Misorientation angles change markedly along each intragranular boundary, linking low- (<10°) and high-angle (10–38°) segments that exhibit distinct misorientation axes and WBV directions. We suggest that these boundaries might be produced by the growth and intersection of individual intragranular boundary segments comprising dislocations with distinct slip systems. There is a fundamental difference between misorientation axis distributions of intragranular boundaries (misorientation axes mostly confined to ice basal plane) and grain boundaries (no preferred misorientation axis). These observations suggest during progressive subgrain rotation, intragranular boundaries remain crystallographically controlled up to large misorientation angles (>>10°). In contrast, the apparent lack of crystallographic control for grain boundaries suggests misorientation axes become randomized, likely due to the activation of additional mechanisms (such as grain boundary sliding) after grain boundary formation, linking boundary segments to encircle a grain. Our findings on ice intragranular boundary development and grain boundary formation may apply more broadly to other rock-forming minerals (e.g., olivine, quartz).

Plain Language Summary

When grains of minerals are placed under high stresses and temperatures, they develop internal (intragranular) boundaries due to the accumulation of crystal defects ("dislocations"). Over time, these boundaries introduce more local rotation ("misorientation") into the crystal structure. Eventually, the amount of rotation becomes large enough that an intragranular boundary evolves into a distinct, new grain boundary. Thus, grains become progressively subdivided during deformation. This process of subdivision allows minerals to weaken, promoting their large-scale flow. To understand intragranular boundary development and grain boundary formation at temperatures close to the melting point, we examined the microstructure of ice samples deformed at −30°C. We found widespread variation in the crystalline structure of individual intragranular boundaries, which cannot easily be explained by previous models for boundary evolution. We propose that intragranular boundaries grow and develop by the progressive coalescence of smaller boundary sections. Furthermore, intragranular boundaries evolve via rotation around specific crystal axes. Intragranular boundaries can transform into grain boundaries, which encloses an area (grain), after rotating beyond a threshold misorientation angle. The grain boundaries are not tied to any specific rotation axis. This implies the introduction of a secondary mechanism (such as sliding along grain boundaries), which serves to disperse crystal orientations.

1. Introduction

To understand the large-scale deformation and bulk strength of crystalline materials, we must examine deformation processes on the microscopic scale. Deformed rock and ice samples commonly exhibit networks of

Writing – review & editing: Sheng Fan, John Wheeler, David J. Prior, Marianne Negrini, Andrew J. Cross, David Wallis

intragranular boundaries—planar defects defined by a sharp change in crystal lattice orientation—that begin developing at very low strains (usually beyond ~2%) and become increasingly widespread as deformation progresses in the plastic field (Fan et al., 2020; Trimby et al., 1998; Valcke et al., 2006; White, 1976). Intragranular boundaries are composed of arrays of dislocations—a type of crystalline line defect that accommodates plastic strain through glide and climb (Orowan, 1934; Polanyi, 1934; Taylor, 1934)—and can be described by a misorientation angle-axis pair. During high-temperature creep, the misorientation angle of a given intragranular boundary increases as dislocations of the same polarity are continuously added, a process termed subgrain rotation (Guillope & Poirier, 1979; Poirier & Nicolas, 1975). Subgrain rotation is often used to explain the formation of subgrain boundaries and kink bands, which are two sub-types of intragranular boundary (Bell et al., 1986; Poirier & Nicolas, 1975; Urai et al., 1986). When the misorientation angle across an intragranular boundary becomes large enough (generally ≥10°), the crystalline structure of the boundary becomes sufficiently disordered that it can no longer be described as a simple array of dislocations. Consequently, the (low-angle) intragranular boundary becomes a (high-angle) grain boundary. This process, subgrain rotation recrystallization, results in the formation of new recrystallized grains at the expense of old, highly strained relict grains. Through subgrain rotation recrystallization, the internal stress state of a material is lowered while the total length of grain boundary per unit volume tends to increase—the corollary being that grain size decreases. Grain size reduction can promote grain size sensitive (GSS) mechanisms such as grain boundary sliding accompanied by dislocation creep and/or diffusion creep (Bestmann & Prior, 2003; De Bresser et al., 2001). In short, subgrain rotation recrystallization can promote strain weakening (via strain energy reduction and activation of GSS mechanisms), which can counteract work hardening due to dislocation multiplication, entanglement, and Hall-Petch (pile-up) effects. Consequently, strain weakening can be achieved, which is necessary (along with the coalescence of weakened zones) for the formation of narrow localized shear zones (Poirier, 1980; Rutter, 1999; Tullis & Yund, 1985).

Intragranular boundaries preserve key information about the dislocations that comprise them (Lloyd et al., 1997; Poirier, 1976; Prior et al., 2002; Trimby et al., 1998) and can be split into two end-member types. Tilt boundaries are composed predominantly of edge dislocations and have misorientation (rotation) axes lying within the boundary plane (Figures 1a and 1b). Twist boundaries, on the other hand, are composed predominantly of screw dislocations, and have misorientation axes perpendicular to the boundary plane (Figures 1c and 1d). Pure twist boundaries need to contain dislocations with at least two distinct Burgers vector directions (Figure 1d).

In this study we present detailed electron backscatter diffraction (EBSD) analyses across intragranular boundaries preserved within deformed coarse-grained (~1,300 μm) ice samples. These samples, which were previously described by Fan, Prior, Hager, et al. (2021), show the widespread development of intragranular boundaries comprised of both high-angle (>10°) and low-angle (4–10°) segments (Figures 2a and 2b). Because the samples are much coarser grained (up to 1,300 μm grain diameter) than our EBSD measuring resolution (5 μm), we are able to resolve intragranular features in fine detail in pursuit of the following goals:

1. Investigating the crystallographic geometry (i.e., misorientation axis-angle pair and dislocation types) of intragranular boundaries formed during high-temperature creep.
2. Understanding how intragranular boundaries evolve as they transform into grain boundaries.

Specifically, we use misorientation, boundary trace (Lloyd et al., 1997) and Weighted Burgers Vector (WBV; Wheeler et al., 2009) analyses to constrain both intragranular boundary structure—that is, misorientation axis and angle—and the types of dislocations that comprise them. These results are used to shed light on the grain scale processes that accompany crystal plastic deformation and strain localization at high homologous temperatures, not only in glacial ices, but also in near-solidus parts of the lithosphere and mantle. In this regard, we treat ice as an analogue for other major rock-forming minerals, namely quartz and olivine. Ice has crystal symmetry very similar to that of quartz (Wilson et al., 2014) and also exhibits strong viscous anisotropy, like olivine (Hansen et al., 2012). Moreover, many rock-forming minerals have melting temperatures that are difficult to reach in the laboratory (e.g., quartz: ~1950 K; olivine: ~2200 K). In contrast, high-temperature ($T_h \geq 0.9$) ice deformation can be easily achieved.

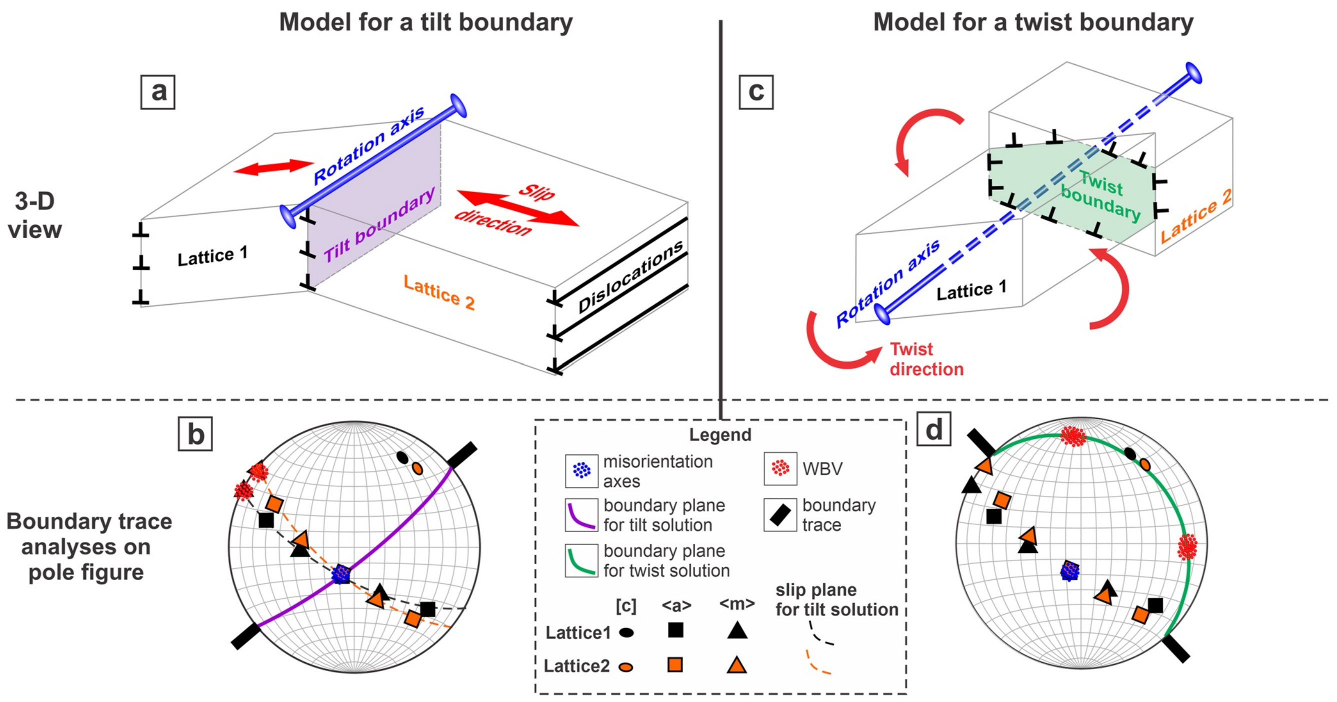

Figure 1. Illustration of principles of the two end-member boundary type models of pure tilt boundary (left column), and pure twist boundary (right column). (a and b) Tilt boundary has misorientation axes (blue dots) lying within the boundary plane (purple great circle). (c and d) Twist boundary has misorientation axes perpendicular to the boundary plane (green great circle), and it needs to contain dislocations with at least two distinct Burgers vector (red dots) directions.

2. Method

2.1. Ice Deformation Experiments and EBSD Data Acquisition

Coarse-grained ice samples—which exhibit a homogeneous microstructure, with few intragranular boundaries and a starting average grain size of ∼1300 μm—were fabricated using a "flood-freeze" method (Cole, 1979). These ice samples were deformed within confined (∼40 MPa) nitrogen gas medium at −30°C under constant displacement rates, yielding true axial strain rates of $\sim 1 \times 10^{-5}$ (sample PIL275) and $6 \times 10^{-5}\,s^{-1}$ (sample PIL271), to ∼10% true axial strain. Full details of the sample fabrication and deformation experiments are provided in (Fan, Prior, Hager, et al., 2021) (see also Appendix A).

We prepared the ice samples for microstructural analysis, and acquired cryo-EBSD data, following the procedures described by Prior and others (2015). EBSD maps were indexed (as ice-1h) at a typical rate of ≥90% under the "speed 2" mode, with a maximum acquisition speed of 1,500 pixels per second. In order to map a representative area of the coarse-grained samples, we collected montage maps by stitching together many smaller EBSD maps (tiles) covering a large total area. Full details of the EBSD data acquisition are provided in Fan, Prior, Hager, et al. (2021), and are summarized in Appendix B.

During sample extraction, transportation, and preparation for cryo-EBSD, post-deformation microstructural modifications may occur. Possible changes include normal grain growth, crystallographic preferred orientation (CPO) evolution, and changes in the geometry—both in sample and crystallographic reference frames—of intragranular boundaries. However, as discussed elsewhere, such changes are likely negligible over the short timescales (within 30 min at $T < -20$°C) involved here (Fan, Prior, Cross, et al., 2021; Fan, Prior, Hager, et al., 2021; Hidas et al., 2017; Wilson et al., 2014).

2.2. EBSD Data Denoising and Grain Construction

Grain construction and denoising were performed using the MTEX toolbox for MATLAB. First, we constructed ice grains from raw EBSD pixel data using a Voronoi decomposition algorithm (Bachmann et al., 2011). In montaged maps, duplicated data points were commonly observed along the boundaries between adjacent tiles

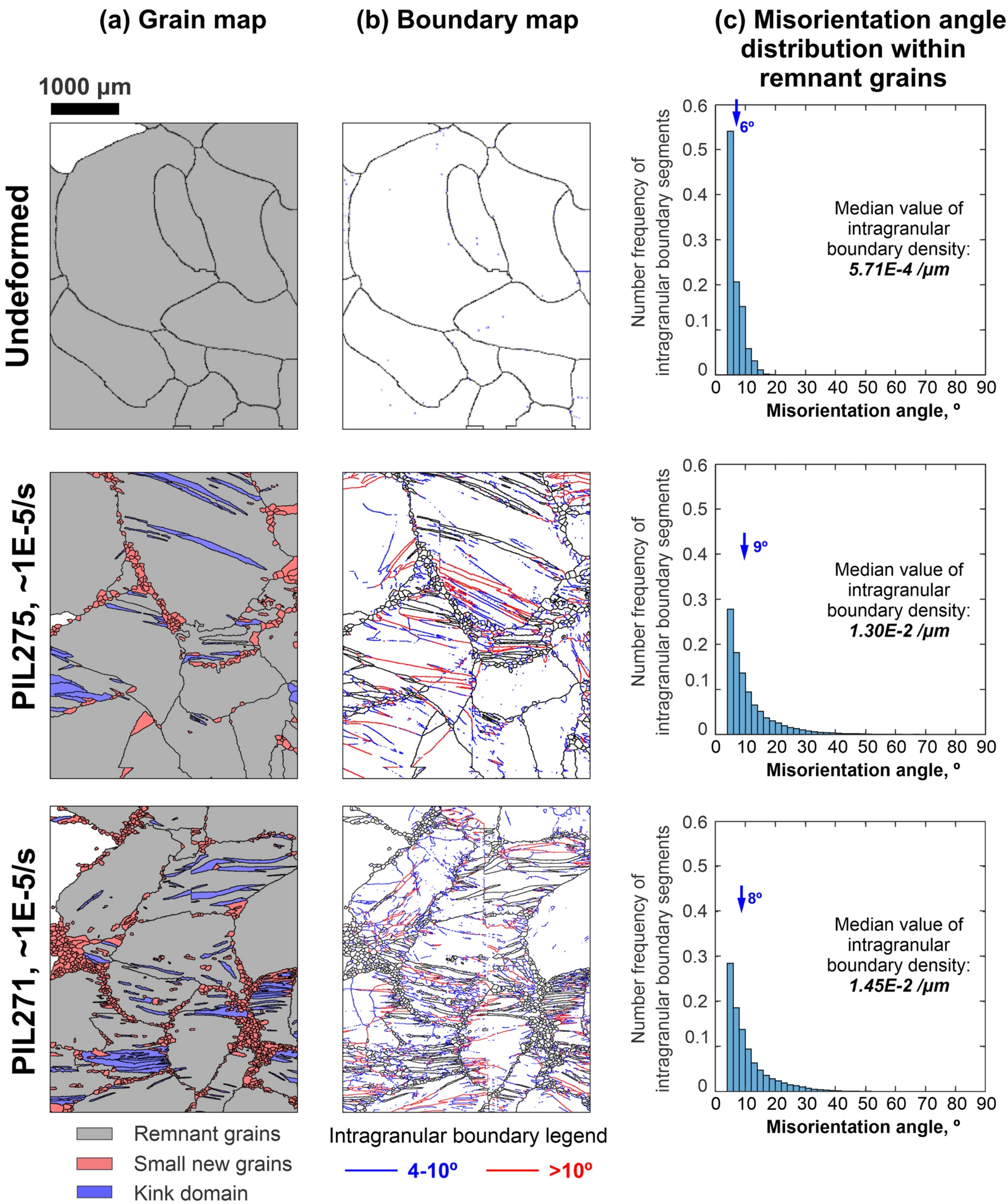

Figure 2. Summary of microstructural statistics for ice samples used in this study. The original data are provided in Fan, Prior, Hager, et al. (2021). (a) Grain map for grain populations. (b) Boundary map. The grain boundary is black. (c) Misorientation angle distribution for intragranular boundaries within remnant grains. The vertical blue arrow represents the median misorientation angle for intragranular boundaries with misorientation angles larger than 4°.

(Fan, Prior, Hager, et al., 2021). These duplicated pixels were removed. Grain boundaries were defined during a first pass of grain construction using a 10° misorientation threshold angle. Mis-indexed pixels (i.e., clusters of fewer than four pixels with the same orientation) and poorly constrained grains (i.e., grains with <50% indexed pixel coverage) as well as pixels belonging to these grains were removed. After that, we applied the MTEX *fill* function on the denoised EBSD data to replace each non-indexed pixel with the nearest pixel indexed as ice-1h. No more than 8% of pixels (by area) were produced during pixel interpolation. Finally, we reconstructed grains using the denoised, interpolated EBSD data, again with a boundary misorientation angle threshold of 10°. This relatively complicated procedure of grain (re-)construction and pixel interpolation was performed in order to fully resolve all pixels along intragranular boundaries. As shown in Appendix C, very few (if any) artifacts are produced by the pixel interpolation procedure.

2.3. Boundary Geometry Analyses

2.3.1. Misorientation Angle and Axes

In this study, we are interested in how misorientation (rotation) angles and axes vary with distance along representative intragranular boundaries. However, because EBSD maps are collected by rastering the electron beam across a sample in a grid-like fashion, the resulting grain maps appear pixelated. As such, grain boundaries suffer from a "staircasing" effect that overestimates their total length (Figures 3a and 3b). To address this issue, we extracted the misorientation angle-axis and *x*–*y* coordinates of the mid-point (red triangle in Figure 3a) of each boundary element. The distance between the mid-points of adjacent boundary elements is then summed (Figure 3a) so that we can plot misorientation angle as a function of distance along the boundary from a reference starting point (e.g., black square mark in Figure 3b) (Figure 3c).

Boundaries with lower misorientation angles produce higher angular errors on misorientation axes (Prior, 1999). Figure 3d illustrates the maximum angular errors of representative misorientation axes with different misorientation angles (from table 2 of Prior (1999)). To minimize uncertainty, intragranular boundaries with misorientation angles smaller than 4° were not included in the following analyses.

2.3.2. Weighted Burgers Vector (WBV) Analyses

Smooth and sharp changes in crystal lattice orientation can be described in terms of populations of geometrically necessary dislocations (GNDs) required to produce the observed lattice bending (Ashby, 1970). For instance, intragranular boundaries can be described as arrays of GNDs, with each GND in turn described by a glide plane and glide direction (i.e., Burgers vector). To fully characterize intragranular boundaries, we seek to determine the dislocation types (and Burgers vectors thereof) that comprise them. As mentioned above, pure tilt walls are comprised of edge dislocations, with Burgers vectors lying within the boundary, while pure twist walls are comprised of screw dislocations, with Burgers vectors lying perpendicular to the boundary (Figure 1). To distinguish between these two types of boundary, here we employ the weighted Burgers vector (WBV) method, which provides a quantitative and convenient means for sampling Burgers vectors from conventional 2-D EBSD maps (Wheeler et al., 2009).

WBV provides the sum of Burgers vectors over a given 2-D region of interest (Wheeler et al., 2009). Specifically, WBV measures the density of dislocation lines that intersect with the mapped 2-D section, multiplied by the associated Burgers vector(s) and has units of (length)$^{-1}$. Dislocation lines lying within the plane of the section (or at low angles to it) have zero (or a smaller) intersection density than dislocation lines perpendicular (or at a high angle) to the section. Thus, WBV is weighted toward dislocations that lie high angles to the section of interest.

For each pixel, we calculated the "differential" form of WBV from local crystal lattice orientation gradients; the "differential" form uses all indexed pixels within a selected region and provide WBV at each pixel (Wheeler et al., 2009). We note that WBV can also be calculated using an "integral" form, which calculates the average WBV over a selected region using numerical integration (Wheeler et al., 2009). The "differential" and "integral" form of WBV share the same mathematical foundation and are complementary to each other (Wheeler et al., 2009). Thus, in this study, we only present the WBV statistics calculated from the "differential" form.

Figure 3g illustrates the maximum angular error of representative measurements with different WBV magnitudes (||**WBV**||). Measurements with lower ||**WBV**|| generally have greater angular error (Wheeler et al., 2009). For

10.1029/2022JB024497

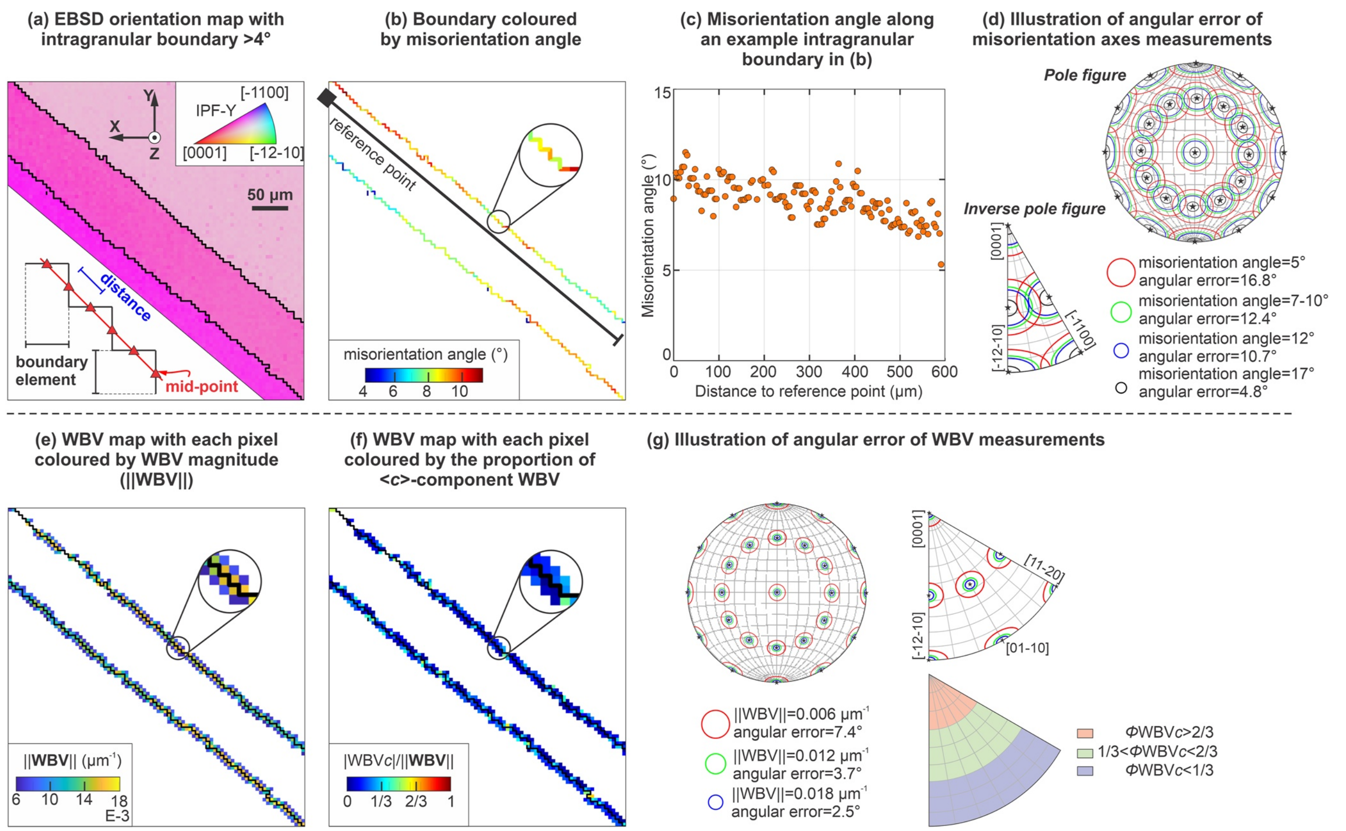

Figure 3. Illustration of principles of misorientation and weighted Burgers vector (WBV) measurement methods applied in this study. (a) Orientation map of a sub-area chosen from the electron backscatter diffraction map of PIL275. Orientation map is colored by inverse pole figure (IPF)-Y, which uses the color map to indicate the crystallographic axes that are parallel to the *y*-axis as shown by the black arrows. Boundaries with misorientation angles higher than 4° are shown black. Measurement of distances between adjacent boundary segments is illustrated in the bottom left corner. (b) Boundary map with each boundary segment colored by the corresponding misorientation angle calculated from full crystallographic axes. (c) Misorientation angle as a function of distance between each boundary segment and boundary segment at the reference point shown in (b). (d) Illustration of maximum angular errors of representative misorientation axes (black dots) adapted from table 2 of Prior (1999). (e) WBV map showing pixels with the magnitude of WBV (||**WBV**||) greater than 0.006 μm^{-1}. These pixels are colored by their corresponding ||**WBV**||. Boundaries are shown black. (f) WBV map showing pixels with ||**WBV**|| greater than 0.006 μm^{-1} colored by the proportion of <*c*>-component WBV (ϕ WBV*c* = |**WBV***c*|/||**WBV**||). Boundaries are shown black. (g) Illustration of maximum angular errors of representative WBVs (black dots) with ||**WBV**|| of 0.006–0.018 μm^{-1} in PF and IPF, and areas in IPF corresponding to different ϕ WBV*c* value ranges.

most analyses in this study, we choose pixels with ||**WBV**|| higher than 0.006 μm^{-1} as a compromise between having enough WBV measurements for statistical significance while minimizing angular error. However, for some of the intragranular structures, we chose pixels with ||**WBV**|| higher than 0.003 μm^{-1} if the number of pixels with ||**WBV**|| > 0.006 μm^{-1} is too small. ||**WBV**|| thresholds of 0.003 and 0.006 μm^{-1} are roughly equivalent to misorientation angles of 1° and 2°, respectively, at an EBSD step size of 5 μm—these values are at least two times higher than the angular uncertainty of conventional EBSD orientation measurement (0.5–1°; Wallis et al., 2016). Moreover, ||**WBV**|| thresholds of 0.003, 0.006 μm, and 0.012 μm^{-1} (equivalent to a misorientation angle of ~3.5°) produce very similar WBV pole figures and inverse pole figures (Section S1 in Supporting Information S1).

WBV analyses do not assume the activity of any particular Burgers vector(s)—WBV can lie anywhere in crystal space (Wheeler et al., 2009). Thus, for each pixel, we can calculate the proportion of WBV lying parallel to a crystal direction of interest. In this case, we are specifically interested in identifying WBV lying parallel to the *c* [0001] axis, WBV*c* (see also Chauve et al., 2017; Piazolo et al., 2015). The ratio between magnitudes of WBV*c* (|**WBV***c*|) and WBV (||**WBV**||)—which we term ϕWBV*c*—enables us to quantify the relative proportion of dislocations gliding within the weak ice basal plane (e.g., Figure 3f). ϕWBV*c* ranges from 0 (for basal WBV lying within the ice basal plane) to 1 (for non-basal WBV lying parallel to the *c*-axis). Following Chauve et al. (2017), we use the thresholds ϕWBV*c* < 1/3, 1/3 < ϕWBV*c* < 2/3, and ϕWBV*c* > 2/3 to separate WBVs that are dominated by <*a*>-component, <*a*+*c*>-component and <*c*>-component, respectively (Figure 3g).

2.3.3. Boundary Trace Analyses

Boundary trace analysis (Lloyd et al., 1997) provides a means for constraining the geometry of an individual boundary segment through knowledge of the boundary rotation (i.e., misorientation) axis, boundary trace (i.e., azimuth of the boundary on a 2-D section), and slip direction (i.e., Burgers vector). Together, these constraints indicate whether a given pair of (misoriented) crystal lattice orientations are more likely separated by either a pure tilt or pure twist boundary (Chauve et al., 2017; Linckens et al., 2016; Piazolo et al., 2008; Prior et al., 2002; Seidemann et al., 2020). For the tilt boundary case, Burgers vectors should lie near-perpendicular to an estimated tilt boundary plane (purple great circle in Figure 1b) containing (a) the intragranular boundary trace (thick black lines; Figure 1b) and (b) misorientation axes for the boundary (blue dots; Figure 1b) on a stereoplot. For the twist boundary case, Burgers vectors should lie within the estimated twist boundary plane (green great circles; Figure 1d) which is a plane lying (a) normal to the boundary misorientation axes (blue dots; Figure 1d) but (b) containing the measured boundary trace (thick black lines, Figure 1d). In many previous studies, Burgers vectors were not independently determined, so trace analyses rested on geometric assumptions about the orientations of the Burgers vector with respect to the boundary trace and misorientation axes (e.g., Seidemann et al., 2020). However, in this study, the Burgers vectors used for boundary trace analyses were independently sampled and determined using the WBV method (Section 2.3.2). Thus, our quantification of intragranular boundary geometry does not contain any assumption about the Burgers vector orientations.

In this study, we select intragranular boundaries that are mostly straight or only slightly curved for analyses, because straight boundaries on 2-D EBSD maps should correspond to approximately planar structures in 3-D (Lloyd et al., 1997, 2021). Intragranular boundaries with irregular geometries in 2-D should represent a probably more sophisticated 3-D crystallographic geometry compared with planar intragranular boundaries analyzed in this study. Fully understanding the slip system of irregular intragranular boundaries will require the input of 3-D boundary geometry and crystallographic orientation data, which can possibly be acquired from the X-ray diffraction contrast tomography technique (e.g., McDonald et al., 2021).

3. Testing the Stereological Impact on Misorientation and WBV Measurements

In this study, we use misorientation and WBV statistics calculated from EBSD data collected from a 2-D surface to understand intragranular boundary geometry in 3-D (Sections 1, 2.2, and 2.3). However, 2-D microstructural data might contain stereological biases that misrepresent the true 3-D structure (Underwood, 1973). Therefore, it is important to test the impact of stereological biases on intragranular distortion measurements (i.e., misorientation and WBV statistics) before these data were used to understand the 3-D geometry of intragranular boundaries.

To test the stereological impact on misorientation and WBV statistics, we extracted a cuboid ice slice from sample PIL271 (Figure 4a) and collected EBSD data from two orthogonal surfaces of the cuboid ice slice following the procedures described in Section 2.2 (Figure 4b). Firstly, we collected EBSD data from a polished surface parallel to the compression axis (“surface 1”) (Figures 4b and 4c). After that, we carefully polished the orthogonal plane of “surface 1” for ∼500 μm; EBSD data were then collected from this second polished surface (“surface 2”), which is normal to compression (Figures 4b and 4c). EBSD pixel maps of “surface 1” and “surface 2” were both colored by crystal orientation with respect to the compression axis (i.e., IPF-σ_1) to aid in the identification of individual grains with clear intragranular boundaries captured on both orthogonal surfaces (Figure 4c). From this procedure, we identified two sets of intragranular boundaries within the surfaces that are parallel and normal to compression using their positions along the intersection line: (a) B1(p) and B1(n); (b) B2(p), B2-1(n), and B2-2(n), where (p) indicates the surface that contains the compression direction (n) indicates the surface normal to compression (Figure 4d).

Figure 5 demonstrates that intragranular boundaries exhibit similar misorientation axes and WBV, regardless of the section orientation:

For B1(p) and B1(n), misorientation axes lie sub-parallel to the ice basal plane, generally clustering near the *m*-axes (rows 1, 2; Figures 5a and 5d). Values of ϕWBVc (|**WBV**c|/||**WBV**||) are generally lower than 1/3 across boundary B1 on both orthogonal surfaces (rows 1, 2; Figures 5b and 5f). Many WBVs have directions close to the *a*-axes (rows 1, 2; Figure 5e); however, WBV directions are slightly more scattered on the surface parallel to compression (B1(p)) than on the surface normal to compression (B1(n)) (compare row 1 and row 2; Figure 5e).

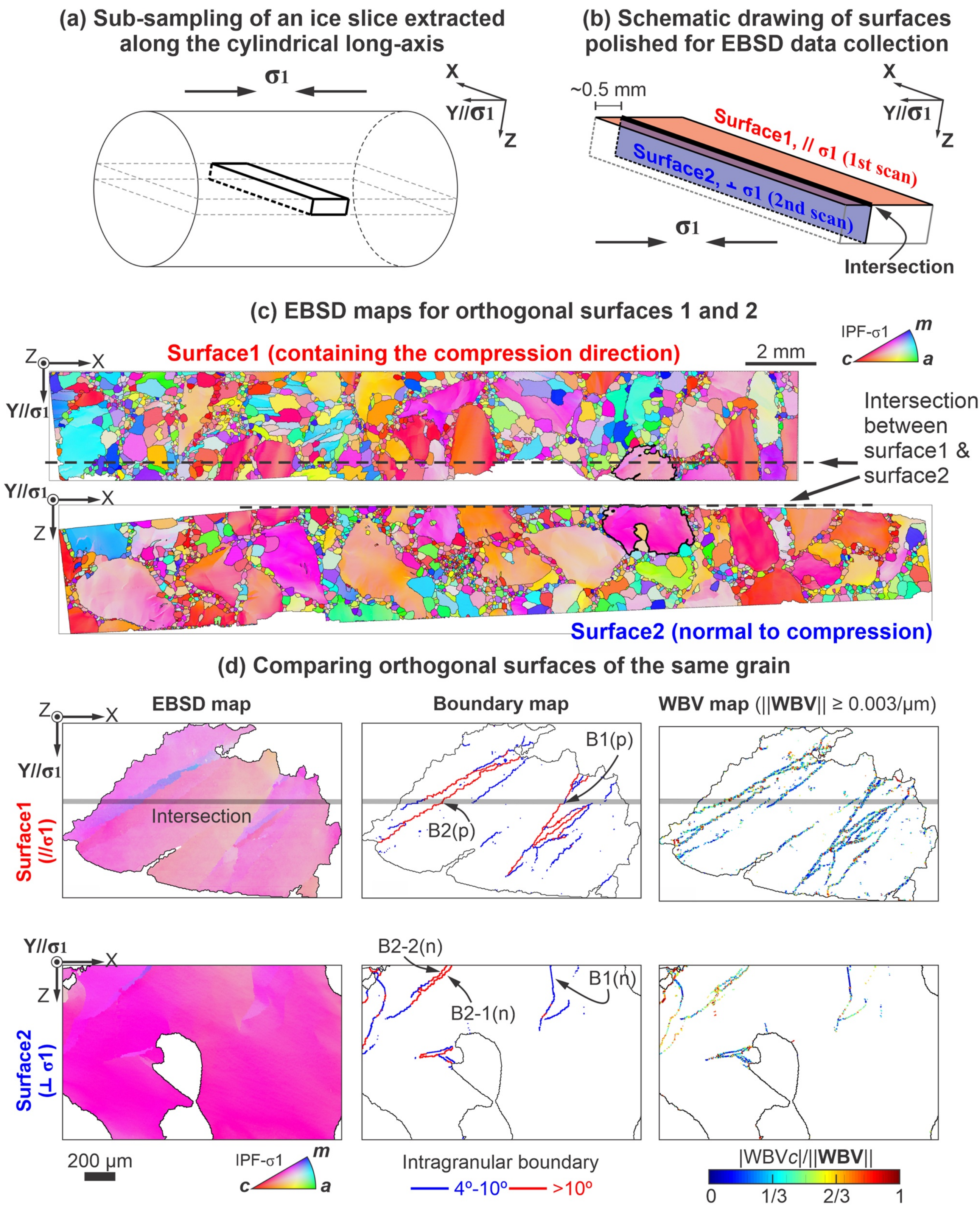

Figure 4. Testing the stereological impact on misorientation and weighted Burgers vector analyses. (a) Schematic drawing showing the geometry of subsampling a cuboid ice slice from sample PIL271. (b) Schematic drawing showing orthogonal surfaces polished for electron backscatter diffraction (EBSD) data collection. (c) EBSD pixel maps of orthogonal surfaces. The EBSD maps are colored by IPF-Y, which uses the color map to indicate the crystallographic axes that are parallel to the shortening axis (y-axis) as shown by the black arrows. (d) Microstructural maps of a grain with clear intragranular boundaries captured on both orthogonal surfaces.

10.1029/2022JB024497

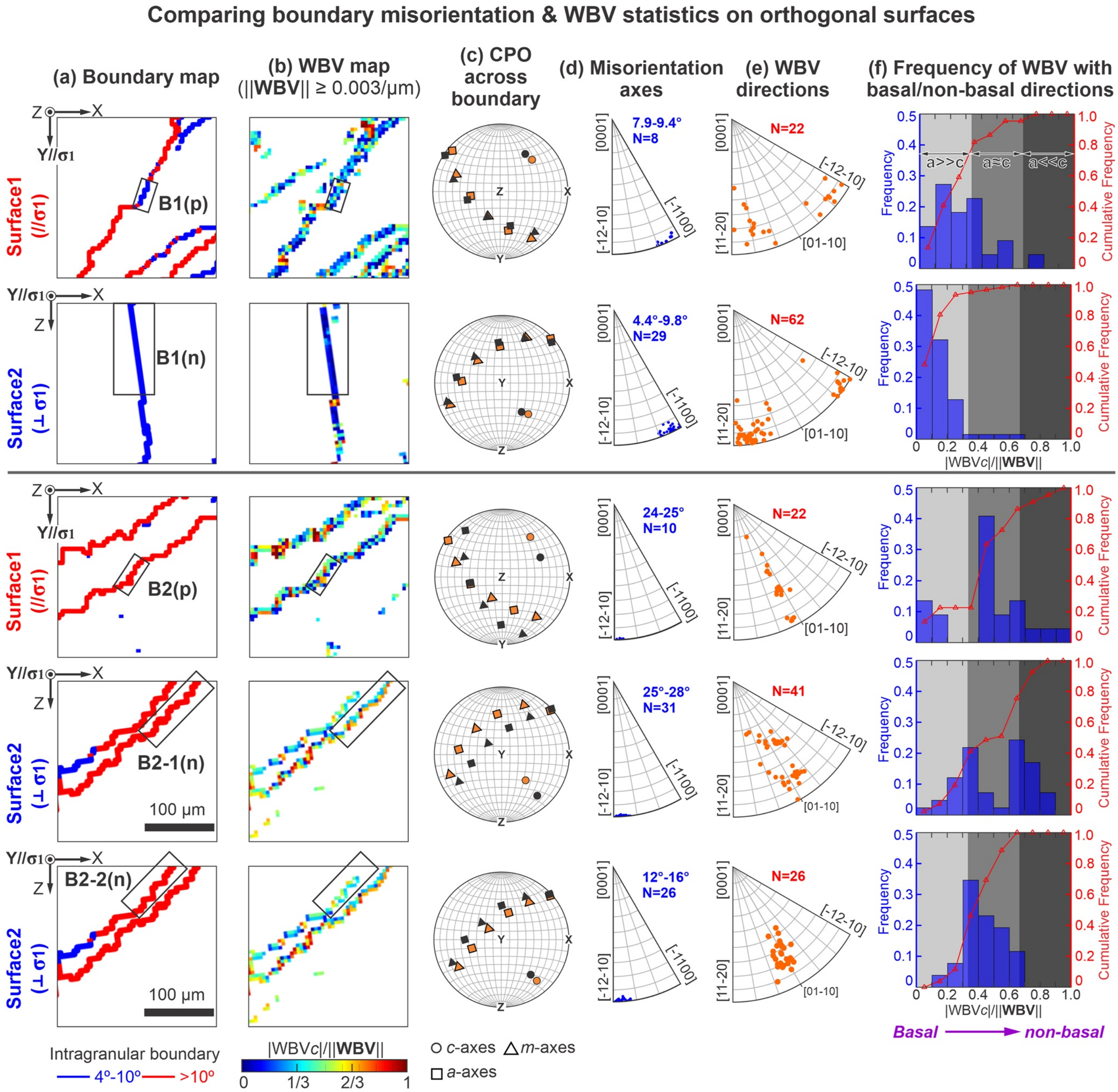

Figure 5. Comparing misorientation and weighted Burgers vector (WBV) statistics across two sets of intragranular boundaries captured on orthogonal surfaces, corresponding to Figure 4(d). (a) Intragranular boundary map with boundary segments colored by their misorientation angles. (b) WBV map. Pixels with ‖**WBV**‖ greater than 0.003 μm^{-1} are colored by their corresponding proportion of <*c*>-component WBV (ϕWBV*c*). The black box illustrates the region selected for crystallographic preferred orientation, misorientation, and WBV analyses. (c) Crystallographic orientations across each intragranular boundary. (d) Misorientation axes of each intragranular boundary with their directions displayed in inverse pole figure (IPF). (e) WBV directions across each intragranular boundary with their directions displayed in IPF. (f) The number frequency and cumulative number frequency distribution of ϕWBV*c* across each intragranular boundary.

For B2(p), B2-1(n), and B2-2(n), misorientation axes also lie sub-parallel to the ice basal plane, but with misorientation axes generally clustering near the *a*-axes (rows 3–5; Figures 5a and 5d). Values of ϕWBV*c* are generally higher than 1/3 on both orthogonal surfaces across boundary B2, with values typically falling between 1/3 and 2/3 (rows 3–5; Figures 5b and 5f). Many WBVs have directions that lie halfway between the ice basal plane and *c*-axis (rows 3–5; Figure 5e).

These observations indicate that misorientation axes and WBV populations (indicated by ϕWBVc) are very similar between orthogonal surfaces. Thus, we assert that stereological bias on misorientation and WBV analyses is negligible. 2-D misorientation and WBV measurements are therefore reliable for understanding the 3-D geometry of individual boundaries.

4. Results: Geometries of Individual Intragranular Boundaries

To understand the processes by which intragranular boundaries evolve during deformation, we perform boundary trace analyses using geometric constraints from misorientation and WBV analyses (Section 2.3). These analyses are performed on representative intragranular boundaries contained within five select grains (Figures 6–10) from two experimentally deformed, coarse-grained ice samples. Figures 6–10 are displayed in the same systematic format, reflecting our generic methodology. In each figure we show:

a. Two overview EBSD maps of intragranular boundaries;
b. Maps that provide:
  - Misorientation angles along specific intragranular boundaries;
  - Misorientation axes along specific intragranular boundaries;
  - The ratio of <c>-component WBV magnitude relative to the total WBV magnitude, ϕWBVc (|**WBV**c|/||**WBV**||), along specific intragranular boundaries;
c. Misorientation angle plotted as a function of distance along a given boundary;
d. Misorientation axis and WBV inverse pole figures, and ϕWBVc histograms; and
e. Boundary trace analyses, to constrain boundary type.

The analyzed intragranular boundaries belong to grains in both hard-slip orientations—with c-axes at ∼30° and ∼80° from the compression axis (Figures 6 and 7)—and easy-slip orientations—with c-axes at ∼45° from the compression axis (Figures 8–10). Intragranular boundaries chosen for analysis were either straight or slightly curved (Figures 6a–10a), for reasons outlined above. Many intragranular boundaries intersect grain boundaries at one or both ends (e.g., B3 in Figure 6a; B4, B5 in Figure 7a; B7 in Figure 8a; B8 in Figure 8a; B9, B10 in Figure 10a), while others do not intersect any grain boundary (e.g., B6 in Figure 7a). Within the representative grains, intragranular boundaries show three types of geometrical compositions, characterized by either (a) one dominant boundary (e.g., Figure 6a), (b) groups of boundaries sub-parallel to one another (e.g., Figures 7a and 10a), and (c) groups of boundaries that crosscut each other (e.g., Figures 8a and 9a). Many of the intragranular boundaries are dominated by a combination of both low-angle (4–10°) and high-angle (>10°) components (e.g., B3–B8; Figures 6a and 6b–9a and 9b). Some other intragranular boundaries are dominated by low-angle components (e.g., B9, B10; Figures 10a and 10b). The microstructural details of these intragranular boundaries are summarized in Table 1.

4.1. Misorientation Angle and Misorientation Axes

More than 50% of all intragranular boundaries within the entire EBSD map have misorientation angles greater than 6–8° (Figure 2c). Misorientation angle changes smoothly and continuously along some of the selected intragranular boundaries (B3–B6, B9, B10; Figures 6b, 6c, 7b, 7c, 10b and 10c), whereas other intragranular boundaries show a sudden change (≥5° within ∼50 μm) of misorientation angle between low- and high-angle components (B7, B8; Figures 8b, 8c, 9b and 9c). Boundaries containing high-angle segments exhibit misorientation angles up to 38° (Figures 9a–9c).

The selected intragranular boundaries have misorientation axes lying mostly within 10° of the ice basal plane (B3–B10; Figures 6d, 7d, 7f, and 8d–10d). Many of the individual boundary components have misorientation axes clustering close to rational crystallographic axes within the ice basal plane—that is, clustering close to the a [11–20] and m [10-10] axes (e.g., B3-2 in Figures 6d and 6e; B4-1, B5-1, B6-1, B6-3 in Figures 7d, 7f, and 7g; B7-1, B7-2, B7-3 in Figures 8d and 8e; B8-1, B8-3 in Figures 9d and 9e). Some other boundary components have misorientation axes that span a range of basal plane orientations between a or m axes (e.g., B3-1 in Figures 6d and 6e; B4-2, B6-2 in Figures 7d, 7f, and 7g; B8-2 in Figures 9d and 9e; B9, B10 in Figures 10d and 10g). For most of the selected intragranular boundaries, the low-angle and high-angle segments have distinct misorientation axis orientations, but they mostly all lie within or very close to the ice basal plane (Figures 6d, 7d, 7f, 8d, and 9d).

10.1029/2022JB024497

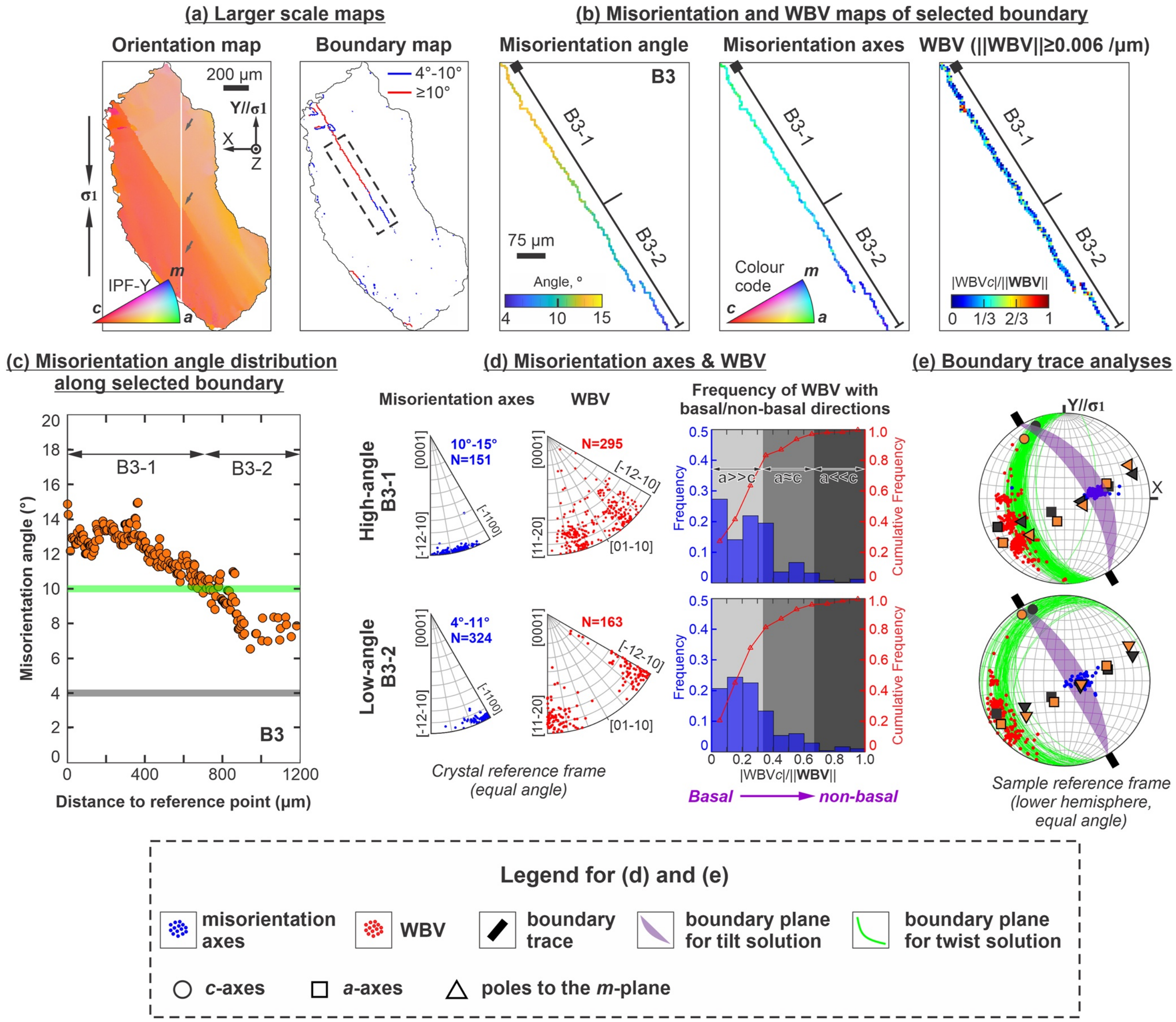

Figure 6. Misorientation and weighted Burgers vector (WBV) analyses of intragranular boundaries developed within a typical grain from PIL275. (a) Orientation map and boundary misorientation angle map. Orientation maps are colored by IPF-Y, which uses the color map to indicate the crystallographic axes that are parallel to the vertical shortening direction (y-axis) as shown by the black arrow. Gray arrow points at eliminated repeated data points at stitches that are montage artifacts (Section 2.2). The black box illustrates the region selected for crystallographic preferred orientation, misorientation, and WBV analyses. (b) Maps that display misorientation angle, misorientation axes, and ϕWBVc across individual intragranular boundary selected in (a). (c) Misorientation angle along individual intragranular boundary displayed in (b). (d) Misorientation axes and WBV directions across components within selected intragranular boundaries with their directions displayed in inverse pole figure. Bar plots show the number frequency and cumulative number frequency distribution of ϕ WBVc across each intragranular boundary component. (e) Boundary trace analyses that include (1) directions of misorientation axes (blue dots) and WBVs (red dots), (2) boundary trace (heavy black bars stick out of primitive circle), (3) estimated range of tilt boundary plane (transparent purple sphere constrained by great circles), and (4) estimated twist boundary solution (thin green great circles that are perpendicular to misorientation axes).

4.2. Weighted Burgers Vectors

For most of the selected individual intragranular boundaries, the low-angle and high-angle components have distinct WBV orientations, albeit mostly confined to the ice basal plane (Figures 6d, 7d, 7f, 8d, and 9d). Thus, most (~60%) WBVs have ϕWBVc (|**WBV**c|/||**WBV**||) values <1/3, indicating a predominance of Burgers vectors lying within the ice basal plane (Figures 6d, 7d, 7f, and 8d–10d). However, high-angle boundary segments have WBVs that are much more dispersed into non-basal orientations than low-angle boundary segments, which

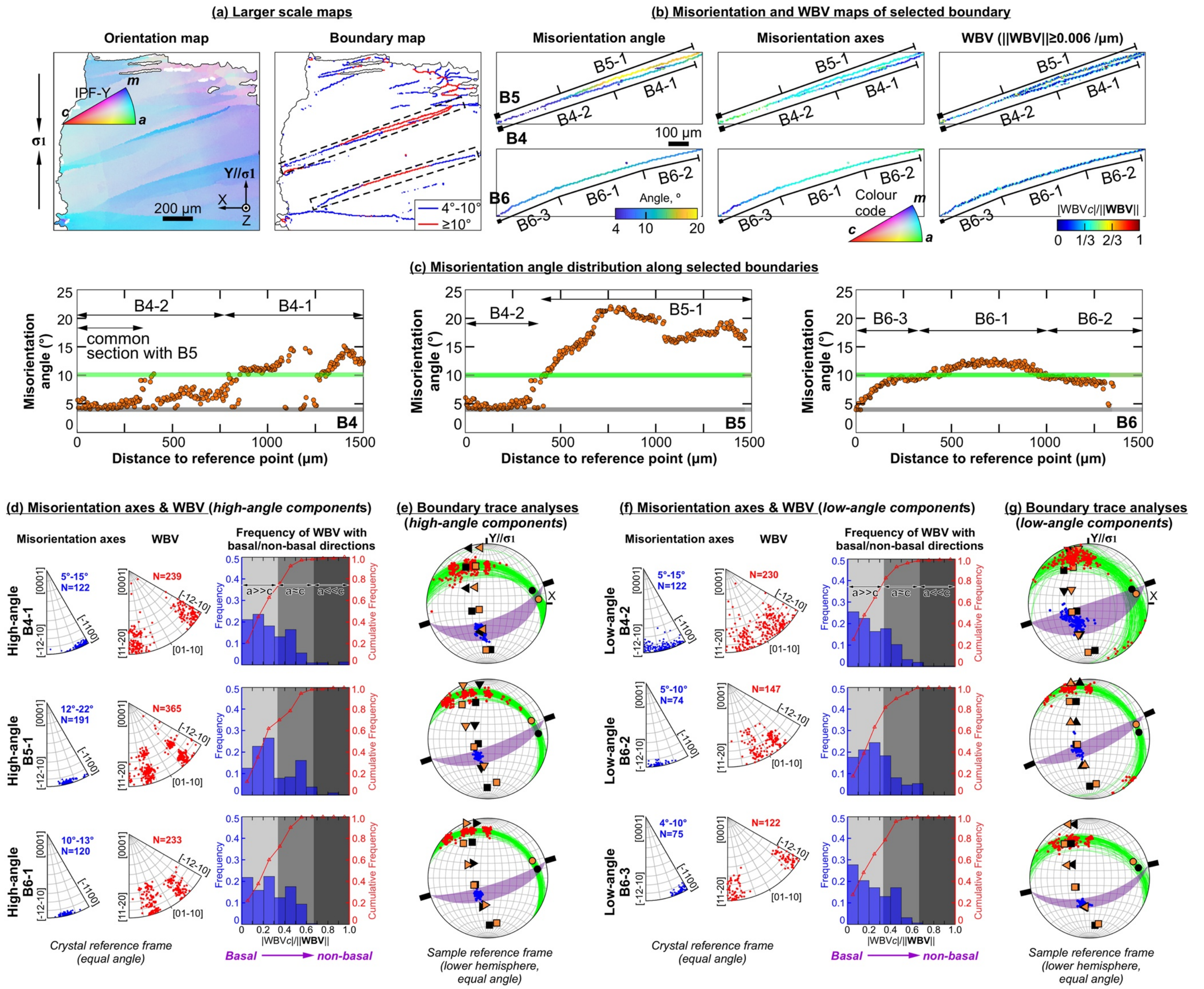

Figure 7. Misorientation and weighted Burgers vector analyses of intragranular boundaries developed within a typical grain from PIL271. Descriptions of (a–c) are the same as Figures 6a–6c. Descriptions of (d and f) are the same as Figure 6d. Descriptions of (e and g) are the same as Figure 6e.

mostly exhibit basal WBVs (Figures 6d, 7d, 7f, and 8d–10d). Consequently, WBV directions become dispersed along great-circle trajectories toward the <*c*>-direction in pole figures (Figures 6e, 7e, 7g, and 8e–10e).

4.3. Boundary Trace Analyses

Pole figures show that WBVs (red dots) across all the selected intragranular boundaries have a smearing of orientations that are generally at 90° to misorientation axes (blue dots). Furthermore, most WBVs lie within (or very close to) planes that contain the boundary trace yet are perpendicular to the boundary misorientation axes (green great circles in Figures 6e, 7e, 7g, and 8e–10e). The smearing of WBVs can extend up to 40–90° along the planes normal to misorientation axes, and in most cases WBVs comprise distinct clusters along this smearing (Figures 6e, 7e, 7g, and 8e–10e).

To examine whether each intragranular boundary more closely represents a pure-tilt or pure-twist boundary end-member, we estimate the boundary plane for:

1. A twist boundary solution (green great circles in Figures 6e, 7e, 7g, and 8e–10e), where the boundary plane lies normal to its misorientation axes, and

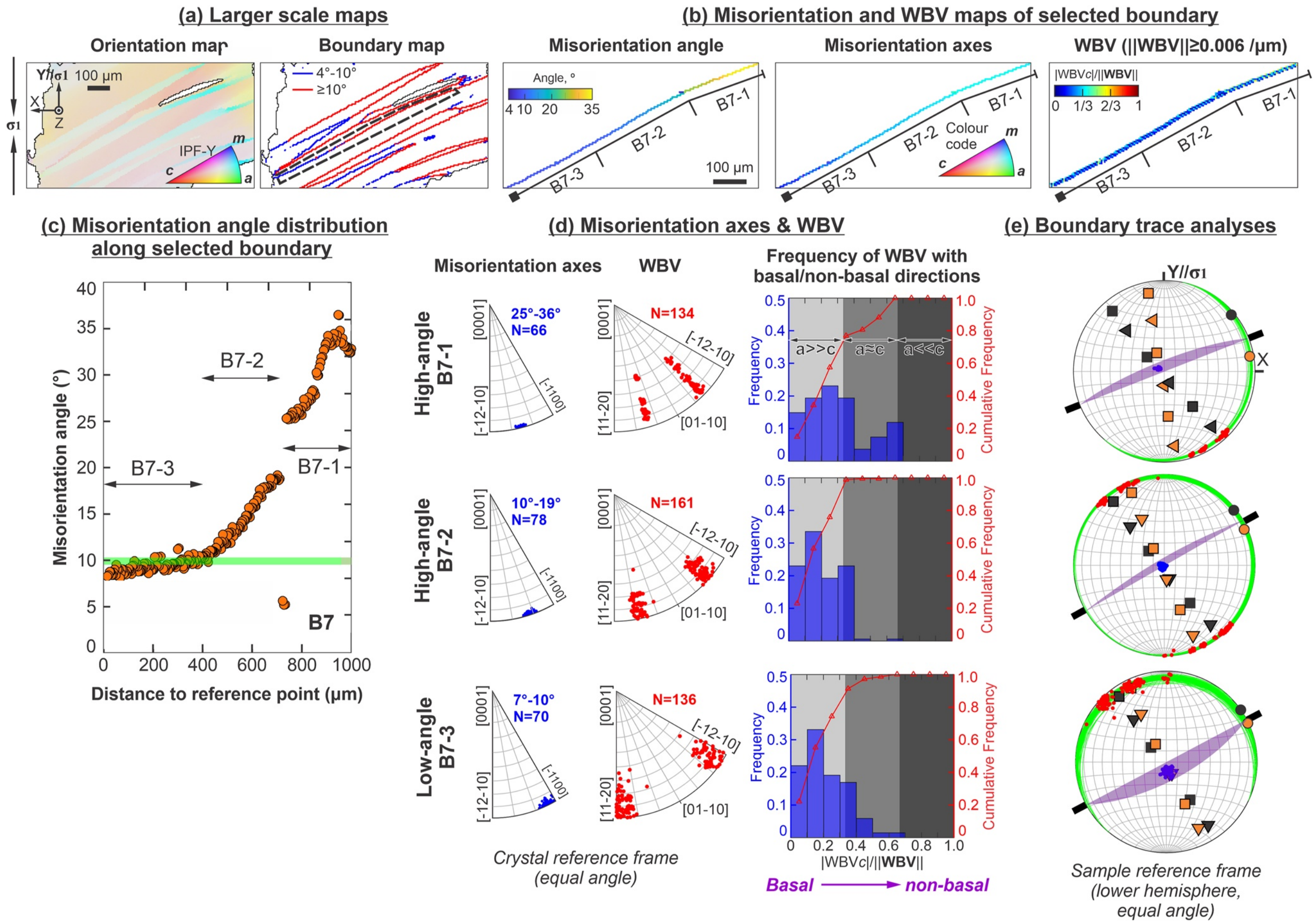

Figure 8. Misorientation and weighted Burgers vector analyses of intragranular boundaries developed within a typical grain from PIL275. Descriptions of (a–e) are the same as Figures 6a–6e.

2. A tilt boundary solution (transparent purple sphere constrained by great circles), which contains the measured 2-D boundary trace and its misorientation axes (Figures 6e, 7e, 7g, and 8e–10e).

For most intragranular boundaries analyzed here, the estimated twist boundary traces lie 10–40° away from the measured 2-D boundary trace (B3 in Figure 6e; B4–B6 in Figures 7e and 7g; B8 in Figure 9e). For the other boundary components, the planes for a twist boundary solution generally coincide with or within 10° to the measured 2-D boundary trace (B7 in Figure 8e; B9, B10 in Figure 10e).

5. Discussion

5.1. Heterogeneous Intragranular Distribution of Dislocations

For all the selected intragranular boundaries, the boundary misorientation axes and WBV across these boundaries have directions that are mostly clustering at rational crystallographic axes (Section 4.1), which are within or very close to the ice basal plane (Figures 6–10; Section 3). The alignment of WBV and/or misorientation axes near rational crystallographic axes are geometrically consistent with the dislocation model—a model in which boundaries are composed of dislocations with rational Burgers vectors (Faul, 2021; Linckens et al., 2016; Piazolo et al., 2015; Weikusat et al., 2017; Wheeler et al., 2009). WBVs across all selected intragranular boundaries have directions that are at 90° to misorientation axes (Section 4.3; Figures 6e, 7e, 7g, and 8e–10e), indicating that Burgers vectors lie sub-perpendicular to the rotation (misorientation) axes, as expected for the hexagonal crystal symmetry of ice (Hondoh, 2000; Nabarro, 1967).

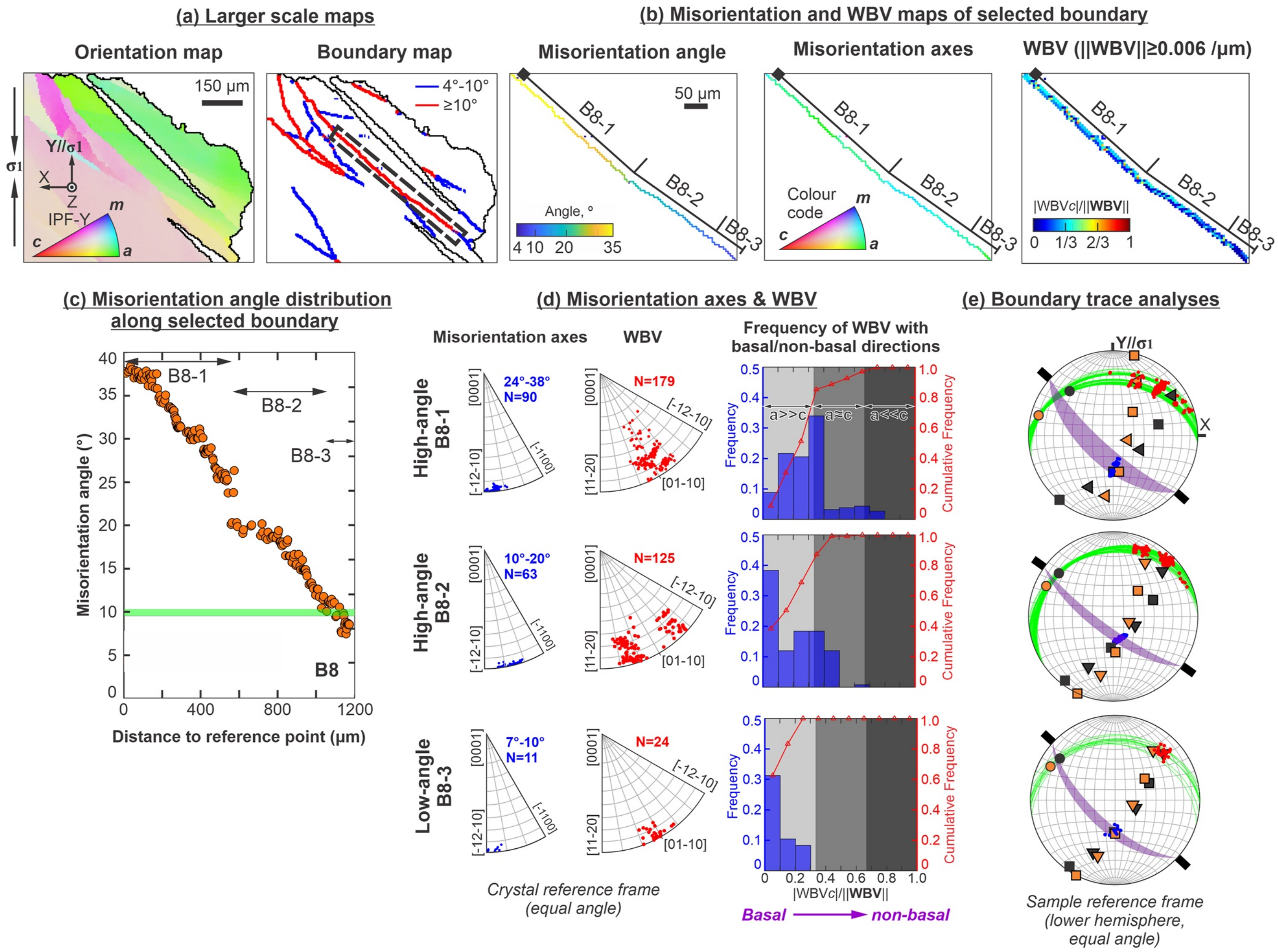

Figure 9. Misorientation and weighted Burgers vector analyses of intragranular boundaries developed within a typical grain from PIL271. Descriptions of (a–e) are the same as Figures 6a–6e.

Intragranular boundaries rarely exhibit a uniform misorientation angle along their length. Instead, misorientation angle changes both gradually and sharply, linking low- and high-angle segments (Section 4.1; Figures 6c–10c). These observations suggest that dislocations are heterogeneously distributed within grains. We suggest that this heterogeneous distribution of dislocations reflects the relatively fast rate of deformation, compared to the rate of dislocation recovery, which ought to be relatively sluggish at the relatively cold conditions of these experiments.

5.2. The Dislocation Make-Up of Intragranular Boundaries

Most of the selected intragranular boundaries—i.e., B3 in Figure 6e; B4–B6 in Figures 7e and 7g; B8 in Figure 9e—have traces of the estimated twist boundary planes at relatively high angles (10–40°) to observed boundary traces (Section 4.3). These boundaries are unlikely to be twist boundaries and are therefore more likely to be tilt boundaries, comprised predominately of edge dislocations (Section 1). WBVs across these boundaries generally form distinct clusters within the ice basal plane (dominated by <*a*>-component) that often smear toward non-basal directions (dominated by <*a*+*c*>- and/or <*c*>-components) (Section 4.2; Figures 6d, 6e, 7d–7g, 8d, and 8e–10e) as previous observed (Chauve et al., 2017; Piazolo et al., 2015). Moreover, the proportion of WBVs with non-basal directions is not negligible (~40%) (Section 4.2; Figures 6d, 7d, 7f, and 8d–10d). Thus, both basal and non-basal edge dislocations contribute to the development of the tilt boundaries examined here.

A few boundaries have traces consistent with a twist solution (Section 4.3; B7 in Figure 8e; B9, B10 in Figure 10e). However, in each of these cases the tilt solution also provides a very similar boundary trace. Thus, we cannot

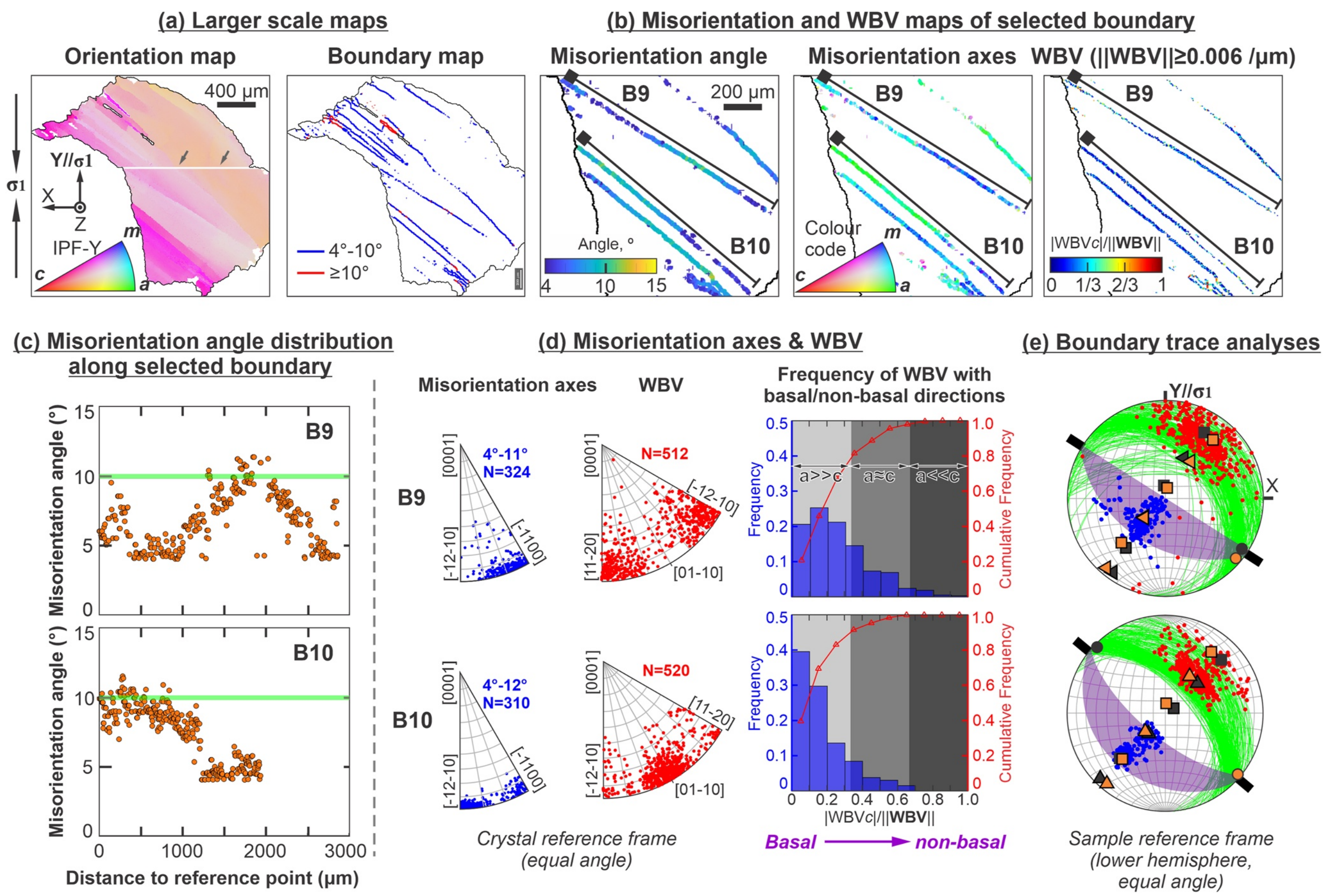

Figure 10. Misorientation and weighted Burgers vector analyses of intragranular boundaries developed within a typical grain from PIL275. Descriptions of (a–e) are the same as Figures 6a–6e.

easily determine a specific boundary type. If these boundaries are pure tilt boundaries, they reflect the recovery of both basal and non-basal edge dislocations, as discussed in the previous paragraph. If, on the other hand, these boundaries are pure twist boundaries, they should (due to geometrical constraints) relate to the recovery of screw dislocations with at least two distinct Burgers vectors (see Figures 1c and 1d). Notably, WBVs for these boundaries typically cluster around only one direction (see B7 in Figure 8e; B9, B10 in Figure 10e). As such, these boundaries are difficult to reconcile with a twist boundary model that requires Burgers vectors with at least two distinct directions. However, if these boundaries were pure twist boundaries, then the absence of additional WBV clusters might reflect a stereological bias, particularly since dislocation lines lying within (or close to) the sample surface produce minimal lattice distortion and are therefore difficult to detect. Because as mentioned above, the WBV method is weighted toward dislocation lines at high angles to the analyzed surface. We should note that boundaries comprised of mixed edge and screw dislocations are theoretically possible (Foreman, 1955; Peach & Koehler, 1950; Weertman, 1965), but have been seldom observed (De Kloe, 2001; Konishi et al., 2020). Furthermore, although most intragranular boundaries in our samples appear to be comprised of edge dislocations, boundaries containing screw dislocations may also be present. In any case, our observation of both basal and non-basal dislocations is consistent with von Mises' criterion (von Mises, 1928), which states that isochoric strain cannot be produced by a single slip system; thus, both basal and non-basal dislocations are required.

Dislocation creep in ice is often thought to be rate-limited by the glide of non-basal edge dislocations (Castelnau et al., 2008; Duval et al., 1983; Goldsby & Kohlstedt, 2001). For example, Duval and others (1983) show that for ice single crystals, dislocation glide on the ice basal plane is at least 60 times easier than dislocation glide on non-basal planes. Thus, the considerable proportion of non-basal dislocations observed here may contribute to strain hardening. However, the ice samples examined in this study underwent strain weakening with increasing strain (see Fan, Prior, Hager, et al., 2021). Strain weakening may be accounted for by (a) the alignment of ice

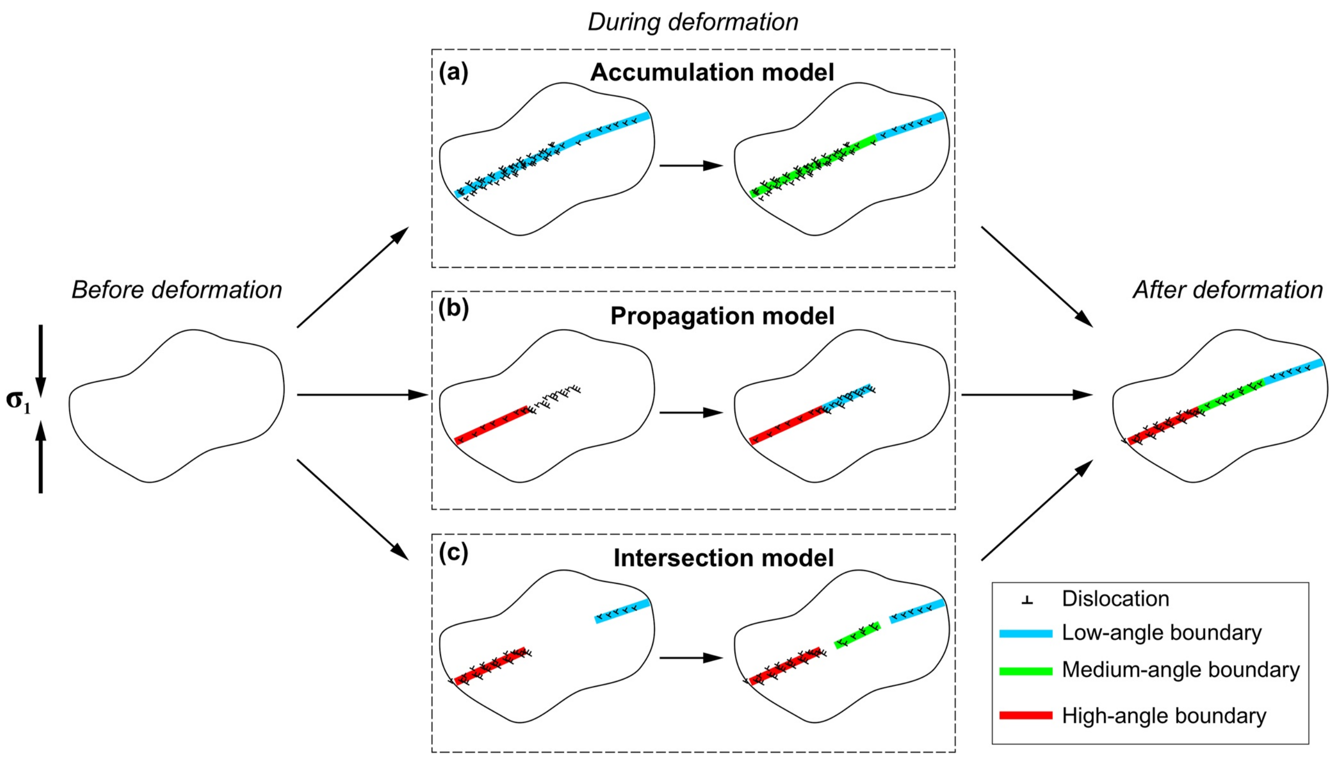

Figure 11. Illustration of possible intragranular boundary development kinematic models that can lead to the formation of identical boundaries composed by low-, medium and high-angle components after deformation. Black non-vertical arrows indicate the sequence of intragranular boundary development. The kinematic models include (a) "accumulation model," (b) "propagation model," and (c) "intersection model".

basal planes into easy-slip orientations, and/or (b) widespread recovery and recrystallization, acting to relax strain heterogeneities, minimize dislocation tangles, and produce soft (initially) strain-free recrystallized grains. In particular, strain-induced GBM is rapid at temperatures close to the ice melting point, and can promote strain weakening via the preferential growth of grains in easy-slip orientations (Fan, Cross, et al., 2021). Therefore, mechanical hardening will likely be counteracted by strain-weakening processes, including crystallographic preferred orientation development and dynamic recrystallization.

5.3. Kinematic Models for Intragranular Boundary Development

Most of the analyzed intragranular boundaries have both low-angle and high-angle components (Section 4.1; Figures 6b–9b). Even though low- and high-angle components were segregated by an arbitrary threshold angle—10°, as is commonly used for minerals—they nevertheless exhibit distinct orientations of misorientation axes and WBV directions (Sections 4.1 and 4.2; Figures 6d, 7d, 7f, 8d, and 9d). Thus, low- and high-angle intragranular boundary segments appear to have distinct crystallographic structures and may therefore form via different processes. Previous studies provide two kinematic models to explain the formation of intragranular boundaries comprising components with both low- and high-angle segments:

1. "Accumulation model" (Figure 11a), which suggests that low-angle boundaries exert a greater attractive force on free dislocations than high-angle boundaries (Kapoor & Verdhan, 2016). Consequently, misorientation across pre-existing low-angle boundaries will increase as deformation progresses and dislocations are continuously added (Wang et al., 2020).
2. "Propagation model" (Figure 11b), which suggests that dislocations will more easily pile up in front of intragranular boundaries with relatively large misorientation angles (Hu et al., 2018). Consequently, high-angle intragranular boundaries can propagate (and growth in length) more effectively as they become more mobile during deformation.

Table 1
Summary of the Intragranular Boundary Information From Figures 6–10

Figure no.	Grain information: Sample no.	Grain information: Angle between grain c-axes and $\sigma 1$	2-D intragranular boundary geometry	Misorientation angle variation along boundary	Boundary component no.	Misorientation axes close to	Proportion of ϕWBVc < 1/3	Boundary type
6	PIL275	~30°	One dominant boundary	Smooth and continuous change	B3-1	Spanning between *a* and *m*	~80%	Tilt
					B3-2	Rational axes	~80%	Tilt
7	PIL271	~80°	Groups of boundaries sub-parallel to one another	Smooth and continuous change	B4-1	Rational axes	~75%	Tilt
					B4-2	Spanning between *a* and *m*	~75%	Tilt
					B5-1	Rational axes	~60%	Tilt
					B6-1	Rational axes	~70%	Tilt
					B6-2	Spanning between *a* and *m*	~80%	Tilt
					B6-3	Rational axes	~75%	Tilt
8	PIL275	~45°	Groups of boundaries that crosscut each other	Sudden change (≥5° within ~50 μm)	B7-1	Rational axes	~80%	Uncertain, tilt or twist or mixed
					B7-2	Rational axes	~80%	Uncertain, tilt or twist or mixed
					B7-3	Rational axes	~80%	Uncertain, tilt or twist or mixed
9	PIL271	~45°	Groups of boundaries that crosscut each other	Sudden change (~5° within ~50 μm)	B8-1	Rational axes	~75%	Tilt
					B8-2	Spanning between *a* and *m*	~80%	Tilt
					B8-3	Rational axes	~100%	Tilt
10	PIL275	~45°	Groups of boundaries sub-parallel to one another	Smooth and continuous change	B9	Spanning between *a* and *m*	~75%	Uncertain, tilt or twist or mixed
					B10	Spanning between *a* and *m*	~85%	Uncertain, tilt or twist or mixed

However, neither model provides a mechanism by which misorientation axes and slip directions can change during boundary rotation (as in the "accumulation" model) or propagation (as in the "propagation" model). To undergo a change in misorientation axis and/or slip direction during boundary rotation or propagation, boundaries must change their geometry—that is, become more curved or irregular with increasing strain/time. In contrast, the boundaries analyzed in this study are mostly planar, and yet are comprised of several crystallographically distinct segments, each with a different WBV direction and misorientation axis (Section 2.3). To account for this observation, we propose a new kinematic model for intragranular boundary development:

3. "Intersection model" (Figure 11c), whereby an intragranular boundary can develop through the accretion of individual boundary segments, each with a distinct WBV direction and misorientation axis. These separately formed intragranular boundary segments intersect after or during their formation. Thus, the "intersection model" necessarily requires that intragranular boundaries become longer with increasing strain/time.

Intragranular boundaries with linear 2-D geometry can be made up by segments with distinct slip systems (Sections 4.1 and 4.2). Therefore, we speculate that, pre-existed intragranular structures, such as low-angle intragranular boundary and/or distorted lattice, might favor the development of segments with distinct slip systems. As deformation progresses, these boundary segments can extend and intersect along the pre-existed intragranular structures and eventually produce a continuous intragranular boundary.

Intuitively, it might require more energy to form and intersect multiple isolated boundary segments (each with a distinct crystallographic geometry) than, for example, propagate a single pre-existing low-angle boundary. We speculate that high differential stresses, as experienced by the ice samples deformed in this study, might favor the boundary intersection model proposed here. However, we should note that our current data sets are insufficient for resolving the evolution of boundary geometry during and after boundary intersection. Future studies should aim to investigate boundary evolution using in situ observations—from, for example, EBSD (Piazolo et al., 2004; Tokita et al., 2017), X-ray diffraction (Cornelius & Thomas, 2018), or neutron diffraction (Nervo et al., 2016).

5.4. Crystallographic Controls on Grain and Intragranular Boundary Structure

In the samples examined here, intragranular boundaries commonly develop misorientation angles up to ∼20°—and up to 38° in extreme cases—while maintaining a strong crystallographic control; that is, while maintaining misorientation axes and WBV directions clustered around rational crystallographic axes, most commonly *a* and *m* axes (Sections 4.1 and 4.2; Figures 6d, 7d, 7f, and 8d–10d). Such observations suggest that intragranular boundary structure is strongly crystallographically controlled, even at large misorientation angles (>>10°) where boundaries are typically thought to be highly disordered.

To investigate whether grain boundaries are similarly crystallographically controlled, we compare the misorientation axis distribution of intragranular boundaries and grain boundaries in Figure 12. We note that, grain boundaries are boundaries with misorientation angles larger than 10° that fully enclose areas (i.e., grains), whereas intragranular boundaries are non-closing. Boundaries are grouped into bins based on their misorientation angle, with a 5° bin width, to see whether boundary structure changes with increasing misorientation. Only boundaries with misorientation angles up to 30° are analyzed, since there are very few intragranular boundaries with misorientation angles >30°. As shown in Figure 12, intragranular boundaries and grain boundaries have fundamentally different misorientation axis distributions, regardless of misorientation angle. For intragranular boundaries, misorientation axes lie mostly within the ice basal plane, becoming clustered more strongly around the *a* [11–20] direction as misorientation angle increases (Figure 12). For grain boundaries, on the other hand, misorientation axes are much more randomly oriented, showing only a weak clustering near the ice basal plane (Figure 12). Similar observations have been reported for ice samples deformed under a wider range of temperatures (−10 to −30°C) (Fan et al., 2020). Such observations suggest that subgrain rotation continuously increases the misorientation angle across intragranular boundaries but maintains crystallographically controlled misorientation axes to large misorientation angles. Consequently, there must be other mechanisms leading to a greater spread of misorientation axes in grain boundaries. We propose that boundary misorientation axes randomization arises because grain boundary formation allows other deformation mechanisms—namely, grain boundary sliding—to operate and produce relative grain rotations (Goldsby & Kohlstedt, 1997). Note that since some intragranular boundaries terminate at one or both ends within a grain, sliding on them would not be possible without the introduction of intragranular shear at each end, which might be difficult. Alternatively, spontaneous nucleation (i.e., the nucleation of grains in random orientations (Herwegh & Handy, 1996); may produce recrystallized grains with orientations that are independent from original remnant grains. Spontaneous nucleation would produce a similarly weak or random misorientation axis distribution. However, given that grain boundary misorientation axes cluster around the ice basal plane (albeit weakly), as observed for intragranular boundaries, we find it more plausible that the misorientation axis distribution is progressively weakened via grain boundary sliding.

6. Conclusions

1. To quantify the crystallographic structure of intragranular boundaries in deformed, coarse-grained ice polycrystals, we performed misorientation and weighted Burgers vector (WBV) analyses on planar intragranular boundaries formed during high-temperature (T_h = ∼0.9), high stress (>1 MPa) deformation. Misorientation angle changes both gradually and sharply along any given intragranular boundary, linking both low- (<10°) and high-angle (>10°, up to 38°) segments.
2. To constrain the types of dislocations contained within intragranular boundaries, we used boundary trace analyses to segregate boundaries into tilt (predominately edge dislocation) and twist (predominately screw dislocation) end-member categories. Most intragranular boundaries appear likely to be tilt boundaries, with WBVs generally clustering within the ice basal plane. However, for most of the examined intragranular boundaries,

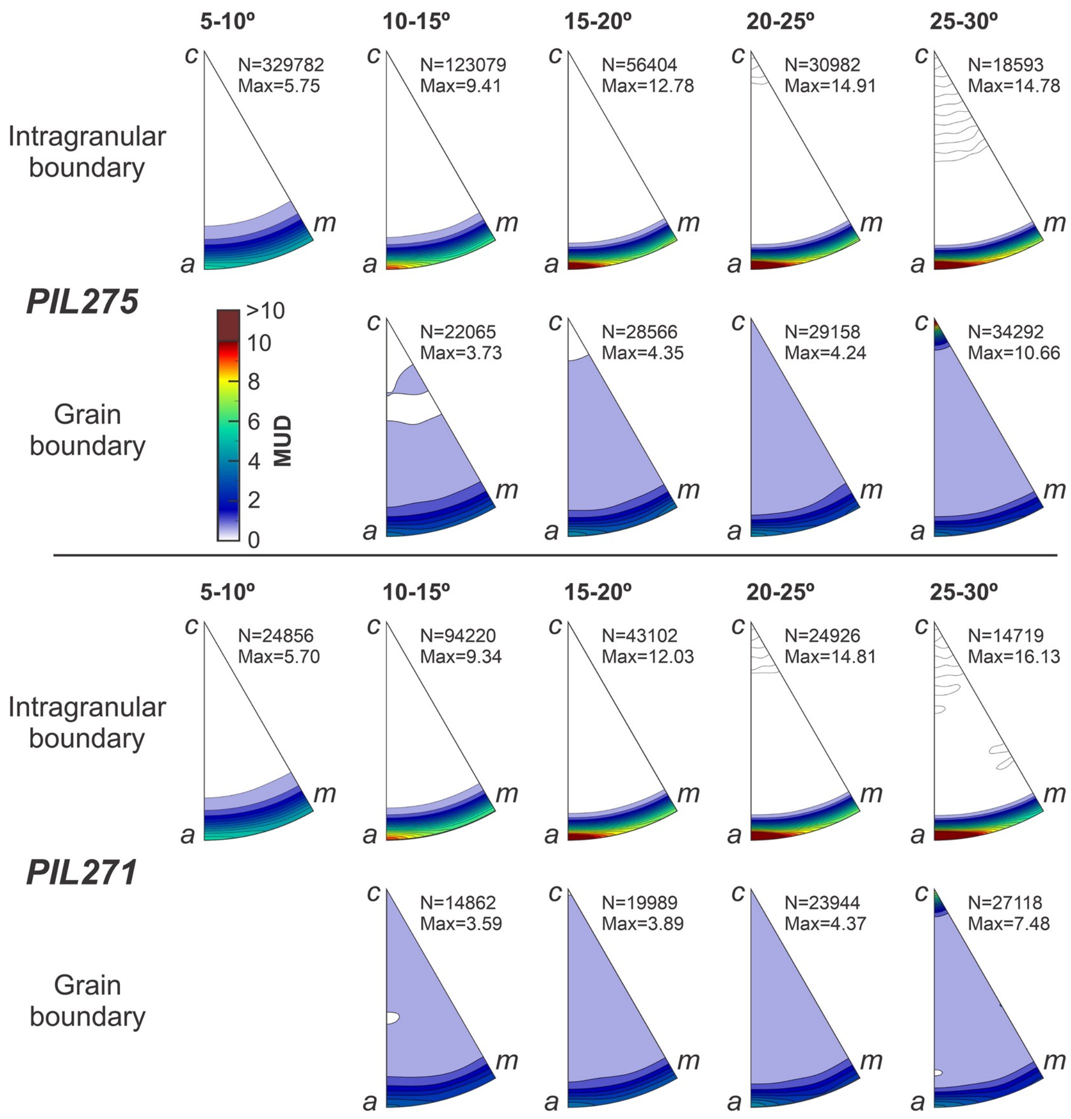

Figure 12. Comparing the misorientation axes distribution with a misorientation angle interval of 5° between intragranular boundaries and grain boundaries of recrystallized grains. The electron backscatter diffraction data set and details for the segregation of recrystallized grains are provided in Fan, Prior, Hager, et al. (2021). The misorientaion axes distributions are displayed as contoured inverse pole figures, with the number of boundary elements (N) and the maximum MUD value (Max) provided at the top right corner.

there is a significant proportion of WBVs in non-basal directions. Thus, mixed basal and non-basal dislocations facilitate intragranular boundary development.

3. Planar intragranular boundaries are comprised of multiple, crystallographically distinct segments, with both low- and high-angle misorientation angles, distinct crystal rotation (misorientation) axes, and distinct WBVs. Previous models for intragranular boundary development cannot account for large variations in boundary structure without invoking significant boundary migration and bending. We therefore propose a new model for intragranular boundary evolution, whereby intragranular boundaries grow through the intersection of multiple crystallographically distinct boundary segments.
4. Misorientation axes of intragranular boundaries lie predominately within the ice basal plane (with misorientation angles up to 38°), whereas the misorientation axes of grain boundaries are much more dispersed. These observations suggest that subgrain rotation—which progressively increases the misorientation angle across intragranular boundaries—can operate to large misorientation angles (>>10°) while maintaining a strong crystallographic control, in terms of rotation around rational crystal axes (mostly commonly, *a* and *m* axes).

Subgrain rotation does not (on its own) produce significant modification (i.e., randomization) of boundary misorientation axes. Instead, boundary misorientation axes become randomized following grain boundary formation. We suggest that this randomization most likely arises from the activation of grain boundary sliding following grain boundary formation.

5. Ice is often considered an analogue for rock-forming minerals such as quartz and olivine (Wilson et al., 2014). Thus, in closing, we suggest that our findings about intragranular boundary evolution may apply more broadly to other rock-forming minerals, particularly those deformed under similarly high homologous temperatures ($T_h = \sim 0.9$) as in this study.

Appendix A: Details of Sample Fabrication and Uniaxial Compression Experiments

A1. Sample Fabrication and Deformation Assembly

Ice seeds with particle sizes of 1.6–2 mm were packed into cylindrical molds (25.4 mm inner diameter) at −30°C. We applied a "wet-sieve" method (Fan, Prior, Hager, et al., 2021)—pouring liquid nitrogen over crushed ice cubes (made from deionized ultra-pure water) while sieving—to remove unwanted fine ice seeds (<300 μm) that are electrostatically clumped on target ice seeds (1.6–2 mm). After that, the packed molds were flooded with degassed, deionized, ultra-pure water at 0°C under vacuum. The flooded molds were then immediately placed vertically on a copper plate for ∼24 hr at −30°C with polystyrene insulating the cylinders from all the other sides. This step ensures that the freezing front migrates slowly upwards, minimizing the entrapment of bubbles within the samples.

Ice samples were gently pushed out from the molds using an Arbor press after ∼24 hr. Ice samples were cut and polished on both ends to limit their lengths to 1.5–2.0 times the sample diameter and to ensure that both ends were flat and perpendicular to the sample cylindrical axis. Each sample was encapsulated in a thin-walled indium jacket tube (∼0.38 mm wall thickness) with the bottom already welded to a stainless-steel end-cap. The top of indium jacket tube was then welded to a steel semi-internal force gauge, with a zirconia spacer placed between the force gauge and sample to thermally insulate the sample during welding. During welding, each sample was kept submerged in a −60°C ethanol bath.

A2. Experimental Process

Ice samples were deformed under uniaxial compression in a cryogenic apparatus (Heard et al., 1990) under ∼40 MPa of nitrogen gas confining pressure in the Ice Physics Laboratory, University of Pennsylvania. The ice samples were deformed at −30°C under constant displacement rates, yielding true axial strain rates of $\sim 1 \times 10^{-5}$ (sample no. PIL275) and $6 \times 10^{-5} s^{-1}$ (sample no. PIL271). The experiments were terminated once the true axial strain reached ∼10%, with the mechanical data (stress-strain and strain rate-strain curves) reported in (Fan, Prior, Hager, et al., 2021). After deformation, the samples were immediately extracted from the apparatus within 15 min, photographed and measured. Samples were progressively cooled to ∼−30, −100, −196°C within ∼15 min and eventually stored in a liquid nitrogen dewar.

Appendix B: Details of EBSD Data Acquisition

Full crystallographic orientation data were collected from each ice sample using the cryogenic electron backscatter diffraction (cryo-EBSD) technique (Iliescu et al., 2004). For each ice sample, a slice with the thickness of ∼5 mm was extracted along the cylinder axis at −20°C within 5 min using a bandsaw. We acquired polished sample surfaces by hand lapping the ice slice, with one side frozen on a copper ingot, at −40°C on sandpapers with grit sizes of 80, 240, 600, 1,200 and 2,400. After polishing, ice-ingot assemblies were stored at liquid nitrogen temperature before being transferred to a scanning electron microscope (SEM) for cryo-EBSD data acquisition.

We collected EBSD data from the polished surface of each ice slice. A Zeiss Sigma VP FEG-SEM combined with an Oxford Instruments' Symmetry EBSD camera was used for the data collection. The ice-ingot assembly was transferred to a cold SEM stage maintained at ∼−100°C. Pressure cycling in the SEM chamber was performed to remove frost and create a damage-free sample surface via sublimation (Prior et al., 2015). We acquired

10.1029/2022JB024497

reconnaissance large-area EBSD maps with a step size of 5 μm at a stage temperature of ∼−95°C, with 2–5 Pa nitrogen gas pressure, 30 kV accelerating voltage and ∼60 nA beam current. Large-area montage maps were constructed by stitching individual frames (EBSD maps) together, using the Oxford Instruments' Aztec software.

Appendix C: Assessing the Impact of EBSD Data Interpolation on Misorientation and WBV Statistics

We used sample PIL271 to assess the impact of EBSD data interpolation on the statistics of misorientation axes and WBVs. In practical, we collected EBSD data from the same surface area (rows 1, 3; Figure C1) using (a) "speed 2" mode with a fast frame rate (maximum ∼1500 Hz), and (b) resolution mode with a slow frame rate (maximum ∼100 Hz). Moreover, we interpolated the EBSD data (details in Section 2.2 collected under "speed 2" mode (row 2; Figure C1). We compared the misorientation and WBV statistics calculated from the same sub-area within (a) raw data collected under "speed 2" mode, (b) interpolated data collected under "speed 2" mode, and (c) raw data collected under "resolution" mode (Figures C1 and C2). We calculated misorientation axes and WBV direction distributions (displayed as IPFs) as well as ϕWBVc distribution (displayed as bar plots; Section 2.3.2 for the whole sub-area as well as individual intragranular boundaries identified within the sub-area (Figure C2). The result shows, the pattern of misorientation axes and WBV distributions are generally very similar amongst raw EBSD data collected under fast and slow frame rates and interpolated EBSD data collected under fast frame rates (Figure C2). This observation suggests the interpolation of EBSD data will introduce insignificant impact on misorientation and WBV statistics.

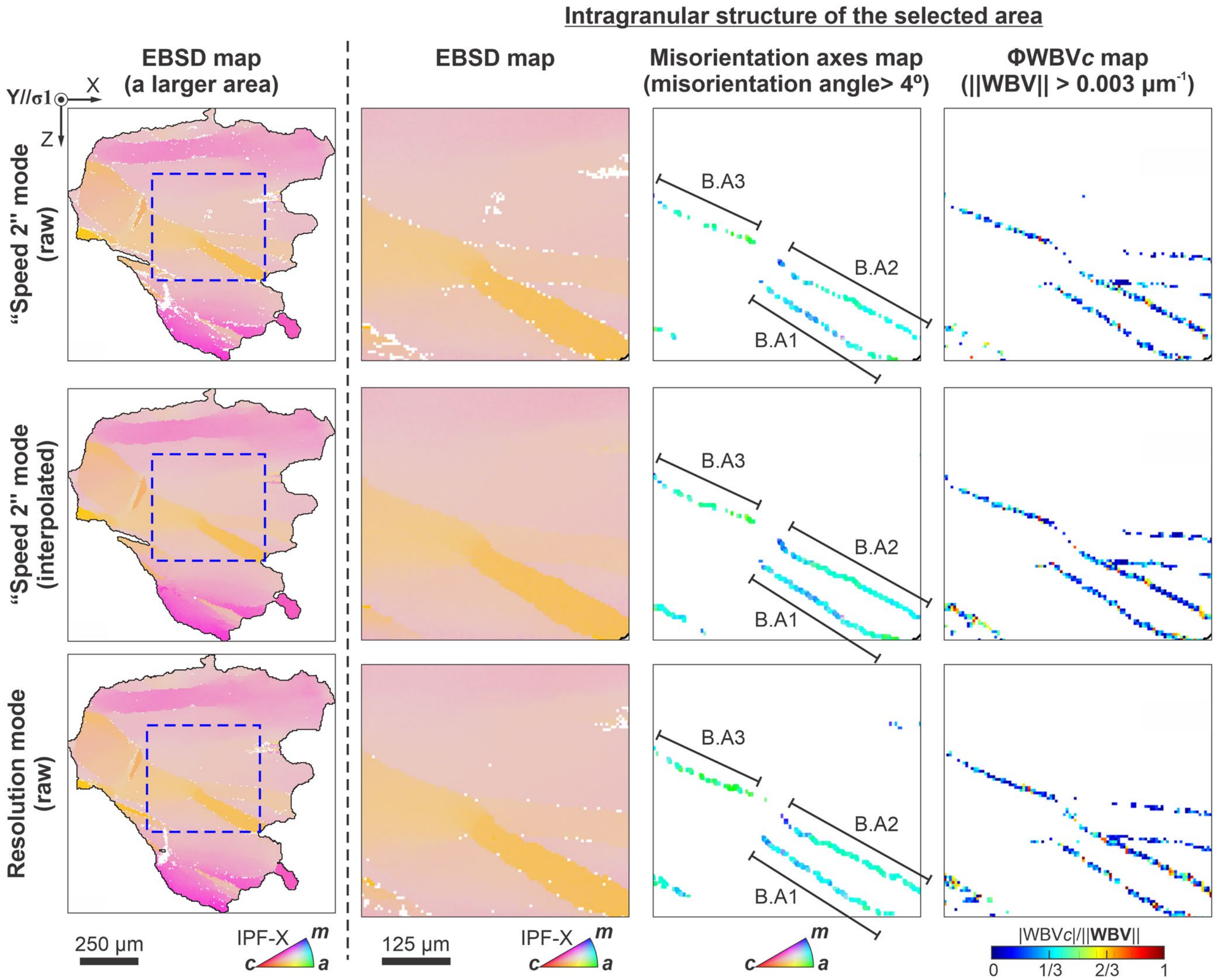

Figure C1. Comparing microstructural maps collected with different speed modes for electron backscatter diffraction (EBSD) data collection. The EBSD maps (columns 1, 2) are colored by IPF-X to favor the identification of intragranular distortion. The first and third rows used raw, un-interpolated EBSD data collected under "speed 2" mode (maximum ∼1500 Hz) and resolution mode (maximum ∼100 Hz). The second row used interpolated EBSD data collected under "speed 2" mode. A selected sub-area (within blue rectangular in Column 1) was chosen for misorientation and weighted Burgers vector analyses (Columns 2–4).

10.1029/2022JB024497

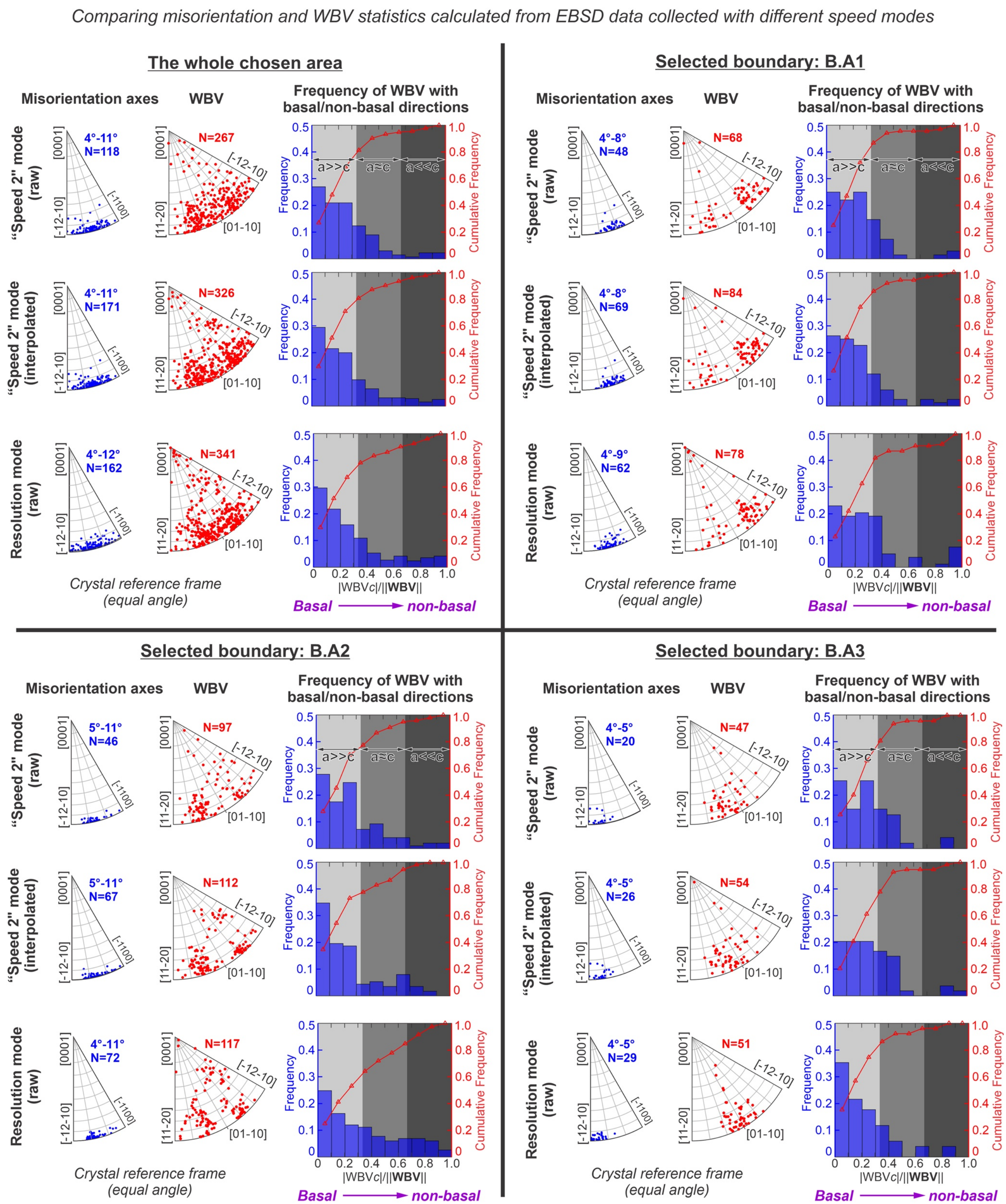

Figure C2. Comparing misorientation and weighted Burgers vector (WBV) statistics for a selected area as well as individual intragranular boundaries displayed in Figure C2. Misorientation axes and WBV directions were displayed in inverse pole figure. Bar plots show the number frequency and cumulative number frequency distribution of ϕWBVc (Section 2.3.2).

Conflict of Interest

The authors declare no conflicts of interest relevant to this study.

Data Availability Statement

Data can be obtained via Mendeley Data (https://doi.org/10.17632/tstn4krkt8.1; Fan et al., 2021).

Acknowledgments

We are thankful to Pat Langhorne for providing the cold-room facility at University of Otago. This work was supported by a NASA fund (Grant No. NNX15AM69G) to David L. Goldsby and two Marsden Funds of the Royal Society of New Zealand (Grant Nos. UOO1116, UOO052) to David J. Prior. Sheng Fan was supported by the University of Otago doctoral scholarship, the Antarctica New Zealand doctoral scholarship, a research grant from New Zealand Ministry of Business, Innovation and Employment through the Antarctic Science Platform (ANTA1801) (Grant No. ASP-023-03), and a New Zealand Antarctic Research Institute (NZARI) Early Career Researcher Seed Grant (Grant No. NZARI 2020-1-5). Open access publishing facilitated by University of Otago, as part of the Wiley – University of Otago agreement via the Council of Australian University Librarians.

References

Ashby, M. F. (1970). The deformation of plastically non-homogeneous materials. *Philosophical Magazine*, *21*(170), 399–424. https://doi.org/10.1080/14786437008238426

Bachmann, F., Hielscher, R., & Schaeben, H. (2011). Grain detection from 2d and 3d EBSD data—Specification of the MTEX algorithm. *Ultramicroscopy*, *111*(12), 1720–1733. https://doi.org/10.1016/j.ultramic.2011.08.002

Bell, I. A., Wilson, C. J. L., McLaren, A. C., & Etheridge, M. A. (1986). Kinks in mica: Role of dislocations and (001) cleavage. *Tectonophysics*, *127*(1–2), 49–65. https://doi.org/10.1016/0040-1951(86)90078-8

Bestmann, M., & Prior, D. J. (2003). Intragranular dynamic recrystallization in naturally deformed calcite marble: Diffusion accommodated grain boundary sliding as a result of subgrain rotation recrystallization. *Journal of Structural Geology*, *25*(10), 1597–1613. https://doi.org/10.1016/S0191-8141(03)00006-3

Castelnau, O., Blackman, D. K., Lebensohn, R. A., & Castañeda, P. P. (2008). Micromechanical modeling of the viscoplastic behavior of olivine. *Journal of Geophysical Research*, *113*(9), 1–18. https://doi.org/10.1029/2007JB005444

Chauve, T., Montagnat, M., Piazolo, S., Journaux, B., Wheeler, J., Barou, F., et al. (2017). Non-basal dislocations should be accounted for in simulating ice mass flow. *Earth and Planetary Science Letters*, *473*, 247–255. https://doi.org/10.1016/j.epsl.2017.06.020

Cole, D. M. (1979). Preparation of polycrystalline ice specimens for laboratory experiments. *Cold Regions Science and Technology*, *1*(2), 153–159. https://doi.org/10.1016/0165-232X(79)90007-7

Cornelius, T. W., & Thomas, O. (2018). Progress of in situ synchrotron X-ray diffraction studies on the mechanical behavior of materials at small scales. *Progress in Materials Science*, *94*, 384–434. https://doi.org/10.1016/j.pmatsci.2018.01.004

De Bresser, J. H. P., Ter Heege, J. H., & Spiers, C. J. (2001). Grain size reduction by dynamic recrystallization: Can it result in major rheological weakening? *International Journal of Earth Sciences*, *90*(1), 28–45. https://doi.org/10.1007/s005310000149

De Kloe, R. (2001). Deformation mechanisms and melt nano-structures in experimentally deformed olivine-orthopyroxene rocks with low melt fractions. Retrieved from http://dspace.library.uu.nl/handle/1874/528

Duval, P., Ashby, M. F., & Anderman, I. (1983). Rate-controlling processes in the creep of polycrystalline ice. *Journal of Physical Chemistry*, *87*(21), 4066–4074. https://doi.org/10.1021/j100244a014

Fan, S., Cross, A. J., Prior, D. J., Goldsby, D. L., Hager, T. F., Negrini, M., & Qi, C. (2021). Crystallographic preferred orientation (CPO) development governs strain weakening in ice: Insights from high-temperature deformation experiments. *Journal of Geophysical Research: Solid Earth*, *126*(12). https://doi.org/10.1029/2021JB023173

Fan, S., Hager, T. F., Prior, D. J., Cross, A. J., Goldsby, D. L., Qi, C., et al. (2020). Temperature and strain controls on ice deformation mechanisms: Insights from the microstructures of samples deformed to progressively higher strains at −10, −20 and −30°C. *The Cryosphere*, *14*(11), 3875–3905. https://doi.org/10.5194/tc-14-3875-2020

Fan, S., Prior, D. J., Cross, A. J., Goldsby, D. L., Hager, T. F., Negrini, M., & Qi, C. (2021). Using grain boundary irregularity to quantify dynamic recrystallization in ice. *Acta Materialia*, *209*, 116810. https://doi.org/10.1016/j.actamat.2021.116810

Fan, S., Prior, D. J., Hager, T. F., Cross, A. J., Goldsby, D. L., & Negrini, M. (2021). Kinking facilitates grain nucleation and modifies crystallographic preferred orientations during high-stress ice deformation. *Earth and Planetary Science Letters*, *572*, 117136. https://doi.org/10.1016/j.epsl.2021.117136

Faul, U. (2021). Dislocation structure of deformed olivine single crystals from conventional EBSD maps. *Physics and Chemistry of Minerals*, *48*(9), 1–15. https://doi.org/10.1007/s00269-021-01157-3

Foreman, A. J. E. (1955). Dislocation energies in anisotropic crystals. *Acta Metallurgica*, *3*(4), 322–330. https://doi.org/10.1016/0001-6160(55)90036-5

Goldsby, D. L., & Kohlstedt, D. L. (1997). Grain boundary sliding in fine-grained Ice I. *Scripta Materialia*, *37*(9), 1399–1406. https://doi.org/10.1016/S1359-6462(97)00246-7

Goldsby, D. L., & Kohlstedt, D. L. (2001). Superplastic deformation of ice: Experimental observations. *Journal of Geophysical Research*, *106*(B6), 11017–11030. https://doi.org/10.1029/2000jb900336

Guillope, M., & Poirier, J. P. (1979). Dynamic recrystallization during creep of single-crystalline halite: An experimental study. *Journal of Geophysical Research*, *84*(B10), 5557–5567. https://doi.org/10.1029/jb084ib10p05557

Hansen, L. N. N., Zimmerman, M. E. E., Dillman, A. M. M., & Kohlstedt, D. L. L. (2012). Strain localization in olivine aggregates at high temperature: A laboratory comparison of constant-strain-rate and constant-stress boundary conditions. *Earth and Planetary Science Letters*, *333–334*, 134–145. https://doi.org/10.1016/j.epsl.2012.04.016

Heard, H. C., Durham, W. B., Boro, C. O., & Kirby, S. H. (1990). A triaxial deformation apparatus for service at 77 ≤ T ≤ 273 K. *The Brittle-Ductile Transition in Rocks*, *56*, 225–228. https://doi.org/10.1029/GM056p0225

Herwegh, M., & Handy, M. R. (1996). The evolution of high-temperature mylonitic microfabrics: Evidence from simple shearing of a quartz analogue (norcamphor). *Journal of Structural Geology*, *18*(5), 689–710. https://doi.org/10.1016/S0191-8141(96)80033-2

Hidas, K., Tommasi, A., Mainprice, D., Chauve, T., Barou, F., & Montagnat, M. (2017). Microstructural evolution during thermal annealing of ice-Ih. *Journal of Structural Geology*, *99*(2086), 31–44. https://doi.org/10.1016/j.jsg.2017.05.001

Hondoh, T. (2000). Nature and behavior of dislocations in ice. *Physics of Ice Core Records*, 3–24.

Hu, Y., Shu, L., Yang, Q., Guo, W., Liaw, P. K., Dahmen, K. A., & Zuo, J. M. (2018). Dislocation avalanche mechanism in slowly compressed high entropy alloy nanopillars. *Communications on Physics*, *1*(1), 1–8. https://doi.org/10.1038/s42005-018-0062-z

Iliescu, D., Baker, I., & Chang, H. (2004). Determining the orientations of ice crystals using electron backscatter patterns. *Microscopy Research and Technique*, *63*(4), 183–187. https://doi.org/10.1002/jemt.20029

10.1029/2022JB024497

Kapoor, R., & Verdhan, N. (2016). Interaction of dislocation pile-up with a low-angle tilt boundary: A discrete dislocation dynamics study. *Philosophical Magazine*, *97*(7), 465–488. https://doi.org/10.1080/14786435.2016.1266102

Konishi, K., Nakamura, Y., Nagae, A., Kawabata, N., Tanaka, T., Tomita, N., et al. (2020). Direct observation and three dimensional structural analysis for threading mixed dislocation inducing current leakage in 4H-SiC IGBT. *Japanese Journal of Applied Physics*, *59*(1), 011001. https://doi.org/10.7567/1347-4065/ab5ee8

Linckens, J., Zulauf, G., & Hammer, J. (2016). Experimental deformation of coarse-grained rock salt to high strain. *Journal of Geophysical Research: Solid Earth*, *121*(8), 6150–6171. https://doi.org/10.1002/2016JB012890

Lloyd, G. E., Farmer, A. B., & Mainprice, D. (1997). Misorientation analysis and the formation and orientation of subgrain and grain boundaries. *Tectonophysics*, *279*(1–4), 55–78. https://doi.org/10.1016/S0040-1951(97)00115-7

Lloyd, G. E., Lee, A. L., & Kahl, M. (2021). A practical method to determine the five-parameter orientation of intragranular boundaries in polycrystals. *Tectonophysics*, *814*, 228955. https://doi.org/10.1016/j.tecto.2021.228955

McDonald, S. A., Burnett, T. L., Donoghue, J., Gueninchault, N., Bale, H., Holzner, C., et al. (2021). Tracking polycrystal evolution non-destructively in 3D by laboratory X-ray diffraction contrast tomography. *Materials Characterization*, *172*, 110814. https://doi.org/10.1016/j.matchar.2020.110814

Nabarro, F. R. (1967). *Theory of crystal dislocations*. Oxford University Press.

Nervo, L., King, A., Fitzner, A., Ludwig, W., & Preuss, M. (2016). A study of deformation twinning in a titanium alloy by X-ray diffraction contrast tomography. *Acta Materialia*, *105*, 417–428. https://doi.org/10.1016/j.actamat.2015.12.032

Orowan, E. (1934). Zur Kristallplastizität. I—tieftemperaturplastizität und Beckersche Formel. *Zeitschrift für Physik*, *89*(9–10), 605–613. https://doi.org/10.1007/BF01341478

Peach, M., & Koehler, J. S. (1950). The forces exerted on dislocations and the stress fields produced by them. *Physical Review*, *80*(3), 436–439. https://doi.org/10.1103/PhysRev.80.436

Piazolo, S., Jessell, M. W., Prior, D. J., & Bons, P. D. (2004). The integration of experimental in situ EBSD observations and numerical simulations: A novel technique of microstructural process analysis. *Journal of Microscopy*, *213*(3), 273–284. https://doi.org/10.1111/j.0022-2720.2004.01304.x

Piazolo, S., Montagnat, M., & Blackford, J. R. (2008). Sub-structure characterization of experimentally and naturally deformed ice using cryo-EBSD. *Journal of Microscopy*, *230*(3), 509–519. https://doi.org/10.1111/j.1365-2818.2008.02014.x

Piazolo, S., Montagnat, M., Grennerat, F., Moulinec, H., & Wheeler, J. (2015). Effect of local stress heterogeneities on dislocation fields: Examples from transient creep in polycrystalline ice. *Acta Materialia*, *90*, 303–309. https://doi.org/10.1016/j.actamat.2015.02.046

Poirier, J. P. (1976). On the symmetrical role of cross-slip of screw dislocations and climb of edge dislocations as recovery processes controlling high-temperature creep. *Revue de Physique Appliquee*, *11*(6), 731–738. https://doi.org/10.1051/rphysap:01976001106073100

Poirier, J. P. (1980). Shear localization and shear instability in materials in the ductile field. *Journal of Structural Geology*, *2*(1–2), 135–142. https://doi.org/10.1016/0191-8141(80)90043-7

Poirier, J. P., & Nicolas, A. (1975). Deformation-induced recrystallization due to progressive misorientation of subgrains, with special reference to mantle peridotites. *The Journal of Geology*, *83*(6), 707–720. https://doi.org/10.1086/628163

Polanyi, M. (1934). Über eine Art Gitterstörung, die einen Kristall plastisch machen könnte. *Zeitschrift für Physik*, *89*(9–10), 660–664. https://doi.org/10.1007/BF01341481

Prior, D. J. (1999). Problems in determining the misorientation axes, for small angular misorientations, using electron backscatter diffraction in the SEM. *Journal of Microscopy*, *195*(3), 217–225. https://doi.org/10.1046/j.1365-2818.1999.00572.x

Prior, D. J., Lilly, K., Seidemann, M., Vaughan, M., Becroft, L., Easingwood, R., et al. (2015). Making EBSD on water ice routine. *Journal of Microscopy*, *259*(3), 237–256. https://doi.org/10.1111/jmi.12258

Prior, D. J., Wheeler, J., Peruzzo, L., Spiess, R., & Storey, C. (2002). Some garnet microstructures: An illustration of the potential of orientation maps and misorientation analysis in microstructural studies. *Journal of Structural Geology*, *24*(6–7), 999–1011. https://doi.org/10.1016/S0191-8141(01)00087-6

Rutter, E. H. (1999). On the relationship between the formation of shear zones and the form of the flow law for rocks undergoing dynamic recrystallization. *Tectonophysics*, *303*(1–4), 147–158. https://doi.org/10.1016/S0040-1951(98)00261-3

Seidemann, M., Prior, D. J., Golding, N., Durham, W. B., Lilly, K., & Vaughan, M. J. (2020). The role of kink boundaries in the deformation and recrystallisation of polycrystalline ice. *Journal of Structural Geology*, *136*, 104010. https://doi.org/10.1016/j.jsg.2020.104010

Taylor, G. I. (1934). The mechanism of plastic deformation of crystals. Part I—Theoretical. *Proceedings of the Royal Society of London—Series A: Containing Papers of a Mathematical and Physical Character*, *145*(855), 362–387. https://doi.org/10.1098/rspa.1934.0106

Tokita, S., Kokawa, H., Sato, Y. S., & Fujii, H. T. (2017). In situ EBSD observation of grain boundary character distribution evolution during thermomechanical process used for grain boundary engineering of 304 austenitic stainless steel. *Materials Characterization*, *131*, 31–38. https://doi.org/10.1016/j.matchar.2017.06.032

Trimby, P. W., Prior, D. J., & Wheeler, J. (1998). Grain boundary hierarchy development in a quartz mylonite. *Journal of Structural Geology*, *20*(7), 917–935. https://doi.org/10.1016/S0191-8141(98)00026-1

Tullis, J., & Yund, R. A. (1985). Dynamic recrystallization of feldspar: A mechanism for ductile shear zone formation. *Geology*, *13*(4), 238. https://doi.org/10.1130/0091-7613(1985)13<238:DROFAM>2.0.CO;2

Underwood, E. E. (1973). Quantitative stereology for microstructural analysis. *Microstructural Analysis*, 35–66. https://doi.org/10.1007/978-1-4615-8693-7_3

Urai, J. L., Means, W. D., & Lister, G. S. (1986). Dynamic recrystallization of minerals. *Mineral and Rock Deformation: Laboratory Studies*, *36*, 161–199. https://doi.org/10.1029/GM036p0161

Valcke, S. L. A., Pennock, G. M., Drury, M. R., & De Bresser, J. H. P. (2006). Electron backscattered diffraction as a tool to quantify subgrains in deformed calcite. *Journal of Microscopy*, *224*(3), 264–276. https://doi.org/10.1111/j.1365-2818.2006.01698.x

von Mises, R. (1928). Mechanik der plastischen Formänderung von Kristallen. *ZAMM—Zeitschrift Für Angewandte Mathematik Und Mechanik*, *8*(3), 161–185. https://doi.org/10.1002/zamm.19280080302

Wallis, D., Hansen, L. N., Ben Britton, T., & Wilkinson, A. J. (2016). Geometrically necessary dislocation densities in olivine obtained using high-angular resolution electron backscatter diffraction. *Ultramicroscopy*, *168*, 34–45. https://doi.org/10.1016/j.ultramic.2016.06.002

Wang, M. J., Sun, C. Y., Fu, M. W., Liu, Z. L., & Qian, L. Y. (2020). Study on the dynamic recrystallization mechanisms of Inconel 740 superalloy during hot deformation. *Journal of Alloys and Compounds*, 820. https://doi.org/10.1016/j.jallcom.2019.153325

Weertman, J. (1965). The Peach–Koehler equation for the force on a dislocation modified for hydrostatic pressure. *Philosophical Magazine*, *11*(114), 1217–1223. https://doi.org/10.1080/14786436508224930

Weikusat, I., Kuiper, E.-J. N., Pennock, G. M., Kipfstuhl, S., & Drury, M. R. (2017). EBSD analysis of subgrain boundaries and dislocation slip systems in Antarctic and Greenland ice. *Solid Earth*, *8*(5), 883–898. https://doi.org/10.5194/se-8-883-2017

10.1029/2022JB024497

Wheeler, J., Mariani, E., Piazolo, S., Prior, D. J., Trimby, P., & Drury, M. R. (2009). The weighted Burgers vector: A new quantity for constraining dislocation densities and types using electron backscatter diffraction on 2D sections through crystalline materials. *Journal of Microscopy*, *233*(3), 482–494. https://doi.org/10.1111/j.1365-2818.2009.03136.x

White, S. (1976). The effects of strain on the microstructures, fabrics, and deformation mechanisms in quartzites. *Philosophical Transactions of the Royal Society A: Mathematical and Physical Sciences*, *283*(1312), 69–86. Retrieved from https://www.jstor.org/stable/74630

Wilson, C. J. L., Peternell, M., Piazolo, S., & Luzin, V. (2014). Microstructure and fabric development in ice: Lessons learned from in situ experiments and implications for understanding rock evolution. *Journal of Structural Geology*, *61*, 50–77. https://doi.org/10.1016/j.jsg.2013.05.006